Unified picture of measurement-induced ionization in the transmon

Marie Frédérique Dumas,[1] Benjamin Groleau-Paré,[1] Alexander McDonald,[1] Manuel H. Muñoz-Arias,[1] Cristóbal Lledó,[1] Benjamin D'Anjou,[1] and Alexandre Blais[1,2]

[1] *Institut Quantique and Département de Physique, Université de Sherbrooke, Sherbrooke J1K 2R1 QC, Canada*
[2] *Canadian Institute for Advanced Research, Toronto, M5G 1M1 Ontario, Canada*

(Dated: February 12, 2024)

Despite the high measurement fidelity that can now be reached, the dispersive qubit readout of circuit quantum electrodynamics is plagued by a loss of its quantum nondemolition character and a decrease in fidelity with increased measurement strength. In this work we elucidate the nature of this dynamical process, which we refer to as transmon ionization. We develop a comprehensive framework which provides a unified physical picture of the origin of transmon ionization. This framework consists of three complementary levels of descriptions: a fully quantized transmon-resonator model, a semiclassical model where the resonator is treated as a classical drive on the transmon, and a fully classical model. Crucially, all three approaches preserve the full cosine potential of the transmon, and lead to similar predictions. This framework identifies the multiphoton resonances responsible for transmon ionization. It also allows us to efficiently compute numerical estimates of the photon number threshold for ionization, which are in remarkable agreement with recent experimental results. The set of tools developed within this work are both conceptually and computationally simple, and we expect them to become an integral part of the theoretical support of all circuit QED experiments.

I. INTRODUCTION

Circuit quantum electrodynamics with transmon qubits is a leading platform for quantum computation [1, 2]. A key feature of this architecture is the dispersive readout where the qubit state is inferred from quadrature measurement of a microwave signal transmitted or reflected from a resonator coupled to the qubit [3]. In principle, increasing the amplitude of the measurement drive, or equivalently the average resonator photon population, should lead to an increase in the measurement's signal-to-noise ratio (SNR). Moreover, because the qubit is strongly detuned from the resonator and thus from the readout drive, the process is expected to be quantum nondemolition (QND) [4].

In practice, however, increasing the readout drive amplitude results in a reduction of the measurement fidelity and to measurement-induced transitions spoiling the QND character of the readout. This is a widely observed phenomenon [5–10]. Although it has been experimentally possible to optimize the dispersive readout to obtain high-fidelity state discrimination [5, 9, 11–14], single-shot qubit readout now lags in fidelity behind the best one- and two-qubit gates [15]. Improving qubit readout is thus an outstanding challenge for the field. Attempts at understanding the origin of these observations have been made using perturbative expansions in the qubit-resonator coupling, qubit anharmonicity or drive amplitudes, while treating the qubit as a two-level system or a Kerr nonlinear oscillator [16–19]. While these approaches highlight important mechanisms for qubit decay and excitation in circuit QED, they do not explain the observed non-QNDness of the dispersive readout. This situation is exacerbated by the fact that no clear parameter dependence for the onset of non-QNDness emerges from experimental observations.

There has recently been a flurry of activity aimed at understanding the origin of the failure of the dispersive readout [6, 7, 20–22]. In particular, numerical simulations of the dynamics of the dispersive readout have shown that the measurement drive, although strongly detuned from the qubit in the dispersive regime, can cause measurement-induced transitions to highly excited states of the transmon at specific resonator photon number [20]. In some cases, this leakage extends to states beyond the transmon's cosine potential well, a phenomenon referred to as transmon ionization. Cohen *et al.* [21] moreover showed that the chaotic behavior of the driven nonlinear classical pendulum can be used to gain qualitative understanding of transmon ionization, an observation which suggests that perturbative methods may not be sufficient to understand ionization. In view of the transmon's negative anharmonicity, the importance of the qubit-resonator frequency detuning, i.e., placing the transmon frequency above or below that of the resonator, was highlighted in Refs. [7, 21].

However, it is unclear how these seemingly disparate approaches relate to each other and whether they make the same quantitative predictions. In this work, we present a unified picture of ionization in the transmon qubit. To do so, we divide the analysis into three main levels of approximation, in all cases considering both positive and negative detuning. We first consider a fully quantized transmon-resonator model which enables us to investigate the mechanisms leading to ionization. We then argue that under typical conditions, a simplified semiclassical model where the resonator is treated as a classical field within Floquet theory is able to accurately predict ionization. Finally, we demote the transmon to a fully classical system and use the Bohr-Sommerfeld quantization rule to make predictions about ionization. Remarkably, we show that all three models lead to simi-

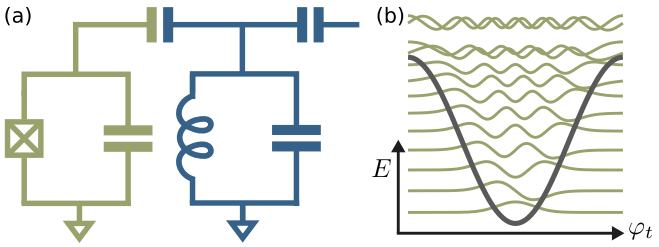

FIG. 1. (a) Schematic of a transmon qubit capacitively coupled to a driven resonator. (b) Cosine potential well of the transmon with $E_J/E_C = 110$ and $n_g = 0$ together with the first 13 eigenstates represented in the phase basis. There are about 9 levels in the well. Transmon states at the bottom of the well are close to eigenstates of the harmonic oscillator while states above the well are close to charge states, i.e., plane waves in the phase basis.

lar predictions for the onset of ionization, and that they agree with experimental results. We also highlight the importance of gate charge in the onset of ionization of the computational states, even deep in the transmon regime [7, 21]. Common to all three approaches is that they consider the full cosine potential of the transmon rather than the common Kerr nonlinearity approximation.

An important feature emerging from all three methods is that there in general exist several critical photon numbers at which ionization can in principle occur. These critical points correspond to resonances that are activated by the strong resonator field due to the Josephson junction's nonlinearity. We show that not all these resonances play an equally important role and that some can be safely ignored in the appropriate conditions. Moreover, we find that the critical photon numbers relevant to ionization are not simply related to the critical photon number $n_{\rm crit}$ of the Jaynes-Cummings Hamiltonian at which the dispersive approximation breaks down [4]. Indeed, while the latter indicates when the qubit-induced nonlinearity becomes important, it is not a good predictor for the onset of ionization. Throughout this work we use the term "ionization" loosely, that is, even if in some instances the measurement-induced transitions do not involve states above the cosine potential well.

II. FULLY QUANTUM MODEL

A. Model

As illustrated in Fig. 1(a) we consider a transmon qubit capacitively coupled to a resonator described by the Hamiltonian ($\hbar = 1$) [1, 2]

$$\hat{H}_{tr} = \omega_r \hat{a}^\dagger \hat{a} + \hat{H}_t - ig(\hat{n}_t - n_g)(\hat{a} - \hat{a}^\dagger), \qquad (1)$$

where ω_r is the bare resonator frequency, g the transmon-resonator coupling strength, and $\hat{a}$ the annihilation operator of the resonator. Moreover, $\hat{H}_t = 4E_C(\hat{n}_t - n_g)^2 - E_J \cos\hat{\varphi}_t$ is the transmon Hamiltonian with E_C the charging energy, E_J the Josephson energy, and n_g the gate charge. The operators $\hat{\varphi}_t$ and $\hat{n}_t$ are the transmon's canonically-conjugate phase and charge operators, respectively. Throughout this work, we assume that the qubit is operated in the transmon regime with $E_J/E_C \gg 1$. Note that we include the often-dropped contribution of the gate charge to the last term of $\hat{H}_{tr}$ to preserve the correct gauge freedom of the Hamiltonian.

The resonator drive used to measure the qubit takes the form

$$\hat{H}_d(t) = -i\varepsilon_d \sin(\omega_d t)\left(\hat{a} - \hat{a}^\dagger\right), \qquad (2)$$

with ε_d the drive amplitude and ω_d the drive frequency. Including single-photon resonator losses, the master equation for the transmon-resonator density matrix is then [1]

$$\partial_t \hat{\rho} = -i[\hat{H}_{tr} + \hat{H}_d(t), \hat{\rho}] + \kappa \mathcal{D}[\hat{a}]\hat{\rho}, \qquad (3)$$

where κ is the resonator decay rate and $\mathcal{D}[\hat{a}]\hat{\rho} = \hat{a}\hat{\rho}\hat{a}^\dagger - \{\hat{a}^\dagger\hat{a}, \hat{\rho}\}/2$ the Lindblad dissipator.

In the absence of drive and qubit-resonator coupling, we denote the eigenstates of the Hamiltonian by $|i_t, n_r\rangle$ where i_t labels the bare transmon eigenstates and n_r labels the bare resonator photon number. The bare energy associated to $|i_t, n_r\rangle$ is $E_{i_t} + n_r\omega_r$, and the transition frequencies between different states of the transmon are denoted $\omega_{i_t j_t} \equiv E_{j_t} - E_{i_t}$. With this notation, the bare qubit transition frequency is $\omega_q = E_{1_t} - E_{0_t}$. The matrix elements of the qubit-resonator coupling are $g_{i_t j_t} = g\langle i_t|\hat{n}_t|j_t\rangle$.

As is usual for quantum information processing in circuit QED, throughout this work we assume that the system is operated in the dispersive limit where $|g/\Delta| \ll 1$ with $\Delta = \omega_q - \omega_r$ the qubit resonator detuning. In that regime, the computational subspace of the qubit is spanned by the dressed ground $|\overline{0_t, 0_r}\rangle$ and excited $|\overline{1_t, 0_r}\rangle$ states of $\hat{H}_0$. Logical operations act on these two dressed states, and it is those states that are resolved in a dispersive qubit measurement. A more precise condition for the dispersive regime to hold is that $\bar{n}_r/n_{{\rm crit},i_t} \ll 1$, where $\bar{n}_r$ is the average resonator photon number and $n_{{\rm crit},i_t}$ is a photon number at which the transmon-resonator interaction stops being dispersive for state i_t (see Appendix A). With the above notation, the commonly used Jaynes-Cummings critical photon number is $n_{{\rm crit},0_t} = |\Delta/2g_{0_t 1_t}|^2$ [1, 4]. As will become clear below, the breakdown of the dispersive approximation during a qubit readout does not necessarily mean that there will be ionization.

Unless otherwise stated, throughout this work we fix the transmon parameters to be $E_J/E_C = 110$ with $E_C/2\pi = 220\,\text{MHz}$. This corresponds to a qubit transition frequency $\omega_q/2\pi = 6.298\,\text{GHz}$, anharmonicity of magnitude $\alpha/2\pi = 240\,\text{MHz}$, and from 9 to 10 levels in the cosine potential well depending on the value of n_g, see Fig. 1(b). Moreover, we take the coupling to

be $g/2\pi = 120\,\mathrm{MHz}$. Due to the negative sign of the transmon's anharmonicity, there is a striking difference in the onset of ionization depending on the sign of the qubit-resonator detuning Δ [7, 21]. In this work, we study both negative and positive detunings. When considering negative detunings, the resonator frequency is $\omega_r/2\pi = 7.5\,\mathrm{GHz}$ ($\Delta/2\pi = -1.202\,\mathrm{GHz}$, $n_{\mathrm{crit},0_t} = 14$, $n_{\mathrm{crit},1_t} = 10.5$) while for positive detuning we take $\omega_r/2\pi = 5.3\,\mathrm{GHz}$ ($\Delta/2\pi = 0.998\,\mathrm{GHz}$, $n_{\mathrm{crit},0_t} = 9.7$, $n_{\mathrm{crit},1_t} = 2.9$). In Sects. III and IV the driven resonator is substituted by a direct drive on the transmon. There, we take $\omega_d/2\pi = 7.515\,\mathrm{GHz}$ at negative detuning and $\omega_d/2\pi = 5.267\,\mathrm{GHz}$ at positive detuning. In both cases, the chosen drive frequency is positioned between the two pulled resonator frequencies corresponding to the qubit's ground and excited states.

Crucially, although they are discussed for those specific sets of parameters, the phenomena we discuss in this article are generic. Once the sign of the detuning Δ has been fixed, the phenomenology for a given choice of parameters is easily understood.

B. Branch Analysis

To understand how the presence of photons in the resonator leads to transmon ionization, we first label dressed states $|\overline{i_t, n_r}\rangle$ by considering which is the closest to the bare transmon state $|i_t\rangle$ at an arbitrary photon number $|n_r\rangle$. Each such sets of states is referred to as a branch. While this identification can easily be done at low photon number, there is no clear such closest state when the photon number approaches or exceeds n_{crit}, where the dressed states are highly entangled qubit-resonator states. To build branches that allow us to gain insight into the dynamics of the driven system at high photon numbers, we instead follow Refs. [20, 23]. In this approach, we use as our starting point the eigenstates $\{|\lambda\rangle\}$ of $\hat{H}_{tr}$ obtained from numerical diagonalization. For each i_t, we identify $|\overline{i_t, 0_r}\rangle$ to be the low-energy eigenstate with the largest overlap with $|i_t, 0_r\rangle$. The branches are built recursively from those starting points and in parallel: given $|\overline{i_t, n_r}\rangle$, the next eigenstate $|\overline{i_t, n_r+1}\rangle$ added to each branch is the one which maximizes the overlap

$$C_{\overline{i_t,n_r}}(\lambda) \equiv |\langle\lambda|\hat{a}^\dagger|\overline{i_t, n_r}\rangle|^2. \tag{4}$$

At each step, $|\lambda\rangle$ is taken from the set of unassigned states. In this way, we obtain branches labeled B_{i_t} corresponding to the set of eigenstates $\{|\overline{i_t, n_r}\rangle\}$ with fixed i_t and n_r spanning the full resonator Hilbert space. When the dispersive approximation is valid, each such branch can thus be pictured as an effective oscillator responding at the pulled resonator frequency associated with the transmon state i_t [20].

The character of the branch eigenstates can be investigated by tracking their average transmon population $N_t \equiv \sum_{i_t,n_r} i_t |\langle i_t|\overline{i_t, n_r}\rangle|^2$ and their average resonator population $N_r \equiv \langle\overline{i_t, n_r}|\hat{a}^\dagger\hat{a}|\overline{i_t, n_r}\rangle$. At very low photon numbers, the dispersive approximation holds and we expect the states within a given branch B_{i_t} to have a transmon population N_t close to the bare value i_t. However, plotting the average transmon and resonator populations parametrically for each branch reveals that this is not always the case, see Fig. 2(a). Instead, a drastic change in the average transmon population N_t is sometimes observed at specific branch-dependent values of N_r, such as a "swapping" of the branches in which two branches exchange their values of N_t. These features are a signature of strong hybridization between transmon states and indicate a complete breakdown of the dispersive approximation. When swapping occurs between a branch linked to computational states and a branch that is near the top of the cosine potential, there is a significant change in the character of the former. It shifts from being predominantly made up of low-energy, localized bare transmon states to being composed largely of high-energy, charge-like bare transmon states. We thus generically refer to this process as ionization.

In Refs. [20, 24], these drastic changes were shown to determine dynamical properties of the system in the presence of a readout drive populating the resonator. The branch analysis thus serves as a diagnosis of the onset of measurement-induced ionization of the transmon. Below, we first focus on negative transmon-resonator detuning, followed by the case where this detuning is positive.

C. Negative detuning $\omega_q < \omega_r$

We consider the case where the qubit frequency is below the resonator frequeny, $\Delta = \omega_q - \omega_r < 0$. To proceed, we note that Eq. (4) can be rewritten as [21]

$$C_{\overline{i_t,n_r}}(\lambda) = g^2 \frac{|\langle\lambda|\hat{n}_t|\overline{i_t, n_r}\rangle|^2}{(E_\lambda - E_{\overline{i_t,n_r}} - \omega_r)^2}. \tag{5}$$

The denominator of this expression conveys that, as expected, when two eigenstates are nearly degenerate dramatic effects such as branch swapping can be expected. But when do we expect dressed states of $\hat{H}_{tr}$ to be near-resonant?

Perturbation theory provides an intuitive answer to this question. Using the usual Schrieffer-Wolff transformation $e^{-\hat{S}}$ with an appropriately chosen $\hat{S}$, one can approximately diagonalize $\hat{H}_{tr}$ as [2]

$$e^{\hat{S}}\hat{H}_{tr}e^{-\hat{S}} \approx \sum_{i_t=0}^{\infty} \left[E_{i_t} + \Lambda_{i_t} + (\omega_r + \chi_{i_t})\hat{a}^\dagger\hat{a}\right] |i_t\rangle\langle i_t|, \tag{6}$$

where Λ_{i_t} are the Lamb shifts and

$$\chi_{i_t} = \sum_{j_t=0}^{\infty} |g_{i_t j_t}|^2 \left(\frac{1}{\omega_r - \omega_{i_t j_t}} - \frac{1}{\omega_r + \omega_{i_t j_t}}\right) \tag{7}$$

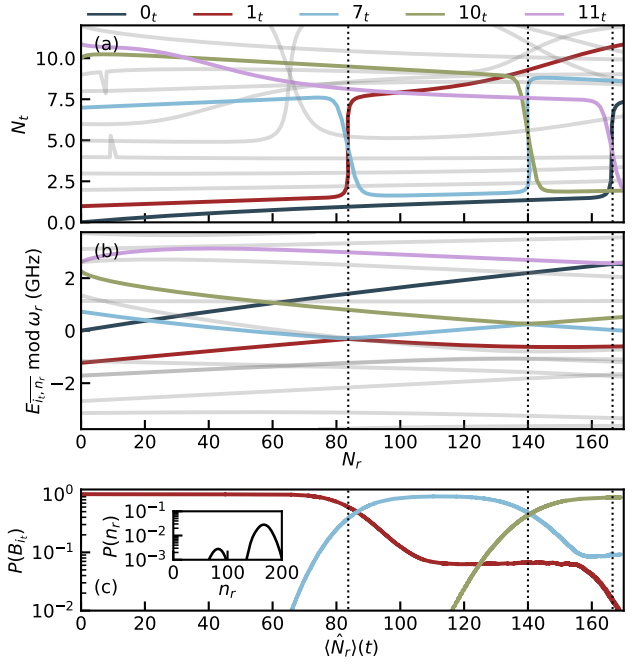

FIG. 2. **Negative detuning.** (a) Average transmon population and (b) modular branch eigenenergies versus N_r for a negative detuning $\Delta/2\pi = -1.202\,\mathrm{GHz}$. Branches B_{0_t}, B_{1_t}, B_{7_t}, B_{10_t} and B_{11_t} are highlighted in color (see legend), the others are gray. Branch population swappings occur at avoided crossings in the modular energy spectrum (vertical dashed lines). (c) Dynamics when initializing in the excited state $|\overline{1_t, 0_r}\rangle$. When the resonator population reaches $\langle \hat{a}^\dagger \hat{a} \rangle \approx 84$ corresponding to the $B_{1_t} - B_{7_t}$ swapping observed in panel (a), the population of the state is mostly transferred to branch B_{7_t}, but a significant part of the population ($\approx 7\%$) stays in branch B_{1_t}, indicating ionization. At $\langle \hat{a}^\dagger \hat{a} \rangle \approx 140$, the population is then mostly transferred to B_{10_t}, corresponding to the $B_{7_t} - B_{10_t}$ swapping in (a), while residual population in B_{7_t} is ionized. Inset in (c) shows in log scale the bimodal Fock state distribution of the resonator at the final time $\kappa t = 2$. For dynamics simulations, we use $\varepsilon_d/2\pi = 180\,\mathrm{MHz}$, $\omega_d/2\pi = 7.515\,\mathrm{GHz}$, and $\kappa/2\pi = 7.95\,\mathrm{MHz}$ (set to match the full χ shift at zero photons). The full-time dynamics were performed using quantum trajectories [25] with 16 transmon states, 300 resonator states, 200 trajectories, and time-evolving up to $\kappa t = 2$.

are the χ shifts obtained here without the usual rotating-wave approximation (RWA) on the transmon-resonator coupling term of Eq. (1) [1]. Importantly, because of the transmon's negative anharmonicity, at negative detuning $\Delta < 0$ the transitions between nearest-neighbor higher-excited states are more off-resonant with the resonator, e.g., $|\Delta - \alpha| > |\Delta|$. This trend continues for all transmon eigenstates i_t within the cosine potential and ensures the validity of perturbation theory at low photon number. Given the small change χ_{i_t} to the dispersion of the resonator, at low photon number we then have a direct mapping between the bare $|i_t, n_r\rangle$ and dressed states $|\overline{i_t, n_r}\rangle \approx e^{-\hat{S}} |i_t, n_r\rangle \equiv |\overline{i_t, n_r}\rangle$.

To understand how this standard analysis helps explain the presence of degeneracies, it is instructive to consider the eigenvalues of $\hat{H}_{tr}$ modulo ω_r. This modular spectrum is plotted versus resonator photon number in Fig. 2(b). At low photon number, the slope of the modular branch energy versus N_r for states in the well is χ_{i_t}, which is positive for states deep in the well and negative for state near the top of the well [26]. At large enough photon number, these opposite ac-Stark shifts can lead to near collisions of the modular energies between states at the bottom and at the top of the well, corresponding to near degeneracies $E_\lambda - E_{\lambda'} \approx 0 \bmod \omega_r$ of the eigenenergies. Nonperturbative corrections to the eigenstates—which arise due to dropped terms in Eq. (6)—turn these near collisions into avoided crossings (dashed vertical lines), see Appendix B. As expected in this situation, the states before and after an avoided crossing swap character. That is, if the eigenenergies of branches B_{i_t} and B_{j_t} collide modulo ω_r, we then have $|\overline{i_t, n_r}\rangle \approx |\overline{i_t, n_r}\rangle$, $|\overline{j_t, n_r}\rangle \approx |\overline{j_t, n_r}\rangle$ before the crossing but $|\overline{i_t, n_r}\rangle \approx |\overline{j_t, n_r + k}\rangle$, $|\overline{j_t, n_r}\rangle \approx |\overline{i_t, n_r - k}\rangle$ after the crossing for some integer k.

These qualitative predictions capture the main features observed in Fig. 2(a,b). As expected, at low photon numbers the modular energies vary linearly with photon number, and the slope is positive for branches corresponding to states deep in the well such as B_{1_t}. On the other hand, the slope is negative for states near the top such as B_{7_t}. An avoided crossing is observed when these two branches eventually meet at $N_r \approx 84$. This is precisely where the branches swap character, see panel (a). The same phenomenology holds for the ground-state branch B_{0_t} which swaps with the charge-like branch B_{11_t} after an avoided crossing at a higher photon number $N_r \approx 166$. An avoided crossing between B_{7_t} and B_{10_t} is also observed at $N_r \approx 140$. Importantly, not all near-degeneracies lead to swapping, such as when B_{0_t} and B_{7_t} cross at around $N_r \approx 23$. This is simply a consequence of the magnitude of the relevant matrix element: at such low photon number it is not possible to efficiently couple the bare 0_t and 7_t states of the transmon via the qubit-resonator coupling, see Appendix B for details.

We stress that although the above leading-order perturbative approach used to interpret Fig. 2 is qualitatively correct, to obtain quantitative predictions one must resort to full numerics. For instance, at large enough photon numbers the self-Kerr of the dressed resonator becomes relevant and must be taken into account when trying to predict the positions of the avoided crossings. In addition, ionization of the ground and excited branches can occur with charge-like states. The modular spectrum of these highly-excited states can vary wildly as a function of photon number, and they can thus become resonant with the computational states. Given that $\hat{n}_t$ can efficiently couple states near the top of the well to each other and even to charge-like states outside the cosine potential [21], this observation is relevant even at

low photon number. Moreover, the charge dispersion of the transmon states near and above the top of the cosine potential well implies that n_g plays a crucial role in determining at which photon number ionization occurs [7, 21]. See Sec. II E for more details on these considerations.

It is worth emphasizing that written in the language of the branch analysis, ionization occurs when the population remains in the ground or excited state branch after the swapping; consider e.g. the red line in Fig. 2(a) which jumps from $N_t \sim 1$ to $N_t \sim 7$ at the anticrossing. This corresponds to an adiabatic transition to a highly-excited transmon state. By contrast, purely diabatic-like transitions between branches do not cause ionization. In practice, the character of the transition can be mixed between these two types of processes. As an illustration, by starting in $|\overline{1_t, 0_r}\rangle$, time-evolving via Eq. (3), and plotting the average population of the branches $P_{B_{i_t}}(t) \equiv \langle \sum_{n_r} |\overline{i_t, n_r}\rangle\langle \overline{i_t, n_r}| \rangle$ as in Fig. 2 (c), we see a nearly full diabatic population transfer from B_{1_t} to B_{7_t} at $\langle \hat{a}^\dagger \hat{a} \rangle \approx 84$, yet the bare transmon population (not shown) does not exceed $N_t \approx 2.75$. The approximately 7% of the population that remains in B_{1_t} after the swapping roughly translates to an equally large probability of ionization. Ionizing by remaining in the ground or excited state branch after the crossing implies a change in the resonator pull, which will in this instance be closer to χ_{7_t} than to χ_{1_t}. As discussed in Ref. [20], this in turn implies that the resonator undergoes a different phase-space trajectory, leading to the bimodal distribution of Fock states as seen in the inset of Fig. 2(c). Note that ionization here happens at photon number that is much larger than the Jaynes-Cummings critical photon number.

The importance of multiphoton resonances as a mechanism causing drive-induced transitions in the transmon has previously been discussed in the literature. Sank *et al.* [6] show that resonances between different excitation-conserving subspaces of the Jaynes-Cummings Hamiltonian mediated by several photons can lead to transmon transitions. That model was able to explain experimentally-observed features. Interestingly, ionization was observed to occur at a photon number significantly larger than the Jaynes-Cummings photon number, as is expected from the above discussion. Moreover, that experiment also shows that while readout-induced transitions occur at specific photon numbers, it is possible to operate the readout at still larger photon numbers. This highlights that, as discussed above, resonances that are traversed diabaticaly do not lead to ionization. Moreover, Xiao *et al.* [22] use a diagrammatic method to compute effective Hamiltonians for a driven transmon in the absence of a resonator. This approach allows them to identify the multiphoton processes that are responsible for drive-induced transmon transitions. In the next section, we show that the model of a directly driven transmon can capture ionization due to a readout drive. The branch analysis unifies these pictures and provide a simple way to predict where resonances occur. It also captures resonances that cannot be obtained via perturbative arguments. This occurs for instance when invoking the RWA for higher-energy states of the cosine potential, which would lead one to incorrectly predict at what photon number ionization occurs, see Sec. II E.

We can now succinctly summarize the three key ingredients leading to ionization of the qubit ground and excited states at negative detuning:

- At low photon number, χ_{i_t} is positive for states deep in the well, leading to an increase in the average energy with photon number. In contrast, transmon states near the top of the cosine potential are pushed down in energy with increasing photon number. Charge-like states above the well can also be pushed down in energy, in a manner which is highly-sensitive to the gate charge.
- These opposite behaviors result in near-degeneracies and thus avoided crossings between these two sets of states at some large-enough photon number, leading to swapping of the transmon branches.
- The resulting hybridization of the transmon's computational state with states at the top or above the well leads to transmon ionization at specific resonator photon number.

D. Positive detuning $\omega_q > \omega_r$

In contrast to negative detuning where branch swapping is observed, at moderate positive qubit-resonator detuning we instead observe that the transmon populations of the branches within the cosine potential well coalesce as the resonator photon number is increased, see Fig. 3(a). Much of the phenomenology associated with this observation stems from the transmon's negative anharmonicity, leading to transitions between neighboring states in the well becoming more resonant with the resonator frequency when climbing the cosine potential. As a result, because of the small anharmonicity of the transmon and for typical large values of g in circuit QED, generically one of the transmon transitions within the well is such that $|E_{i_t+1} - E_{i_t} - \omega_r| \sim g$. For that transition, the dispersive approximation breaks down even at zero resonator photon population. In the Kerr oscillator approximation for the transmon where $\omega_{i_t,i_t+1} \sim \omega_q - i_t\alpha$, this 1-photon resonance occurs for the transmon level $i_t^\star \sim \text{round}[(\omega_q - \omega_r)/\alpha]$ [7].

For example, with the parameters of Fig. 3 we have that

$$\begin{cases} E_{i_t+1} - E_{i_t} > \omega_r & \text{if } i_t \leq 3, \\ E_{i_t+1} - E_{i_t} \approx \omega_r & \text{if } i_t = 4, \\ E_{i_t+1} - E_{i_t} < \omega_r & \text{if } i_t \geq 5, \end{cases} \tag{8}$$

such that $i_t^\star = 4$ is the state for which the dispersive approximation first fails. This is confirmed by examining

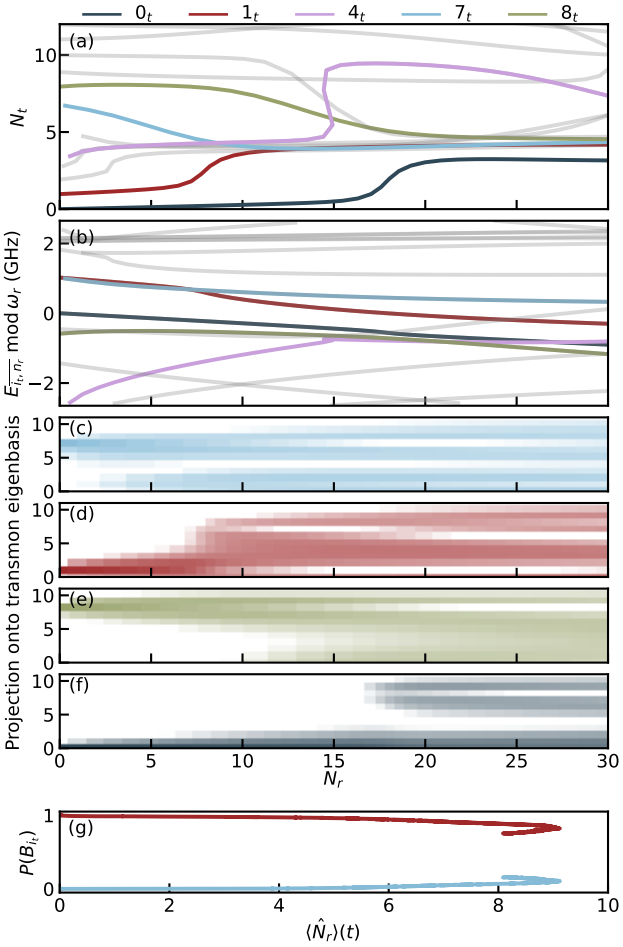

FIG. 3. **Positive detuning.** (a) Average transmon population, (b) modular eigenenergies of branches and (c)-(f) projection of branch eigenstates on the transmon eigenbasis in logarithmic scale versus N_r for a positive detuning $\Delta/2\pi = 0.998\,\mathrm{GHz}$. Branches B_{0_t}, B_{1_t}, B_{4_t}, B_{7_t} and B_{8_t} are highlighted in color (see legend), the others are gray. Branch population bunching is observed about state $i_t^\star = 4$. (g) Dynamically simulated populations of branches 1_t (red line) and 7_t (light blue line) when initializing in the excited state $|\overline{1_t, 0_r}\rangle$. Dynamics simulations are done similarly to Fig. 2(c), but with $\varepsilon_d/2\pi = 93\,\mathrm{MHz}$, $\omega_d/2\pi = 5.267\,\mathrm{GHz}$, $\kappa/2\pi = 11.98\,\mathrm{MHz}$, and 120 resonator states.

the modular energies of the branches, see Fig. 3(b). Unlike the prediction made by the dispersive approximation of Eq. (6), $E_{\overline{4_t,n_r}}$ does not vary linearly at small photon number (pink line), indicating a strong mixing of the bare state $|4_t, n_r\rangle$ with other neighboring bare transmon states. Increasing the photon number, hybridization of $i_t^\star$ with neighboring states leads to level repulsion, and in turn to collisions with other branches.

At the moderate positive detuning considered here, this hybridization is further accentuated by near resonances (modulo ω_r) between pairs of states in the well. For the parameters of Fig. 3, this is the case of the pair of states 1_t and 7_t for which $E_{7_t} - E_{1_t} - 6\omega_r \sim g$, and 0_t and 8_t for which $E_{8_t} - E_{0_t} - 8\omega_r \sim g$. These transitions require multiple intermediate virtual transitions and are thus suppressed at very low photon numbers, see in Fig. 3(b) the almost resonant modular energies of branches 1_t and 7_t running parallel up to $N_r \approx 7$. However, because the coupling matrix elements is proportional to $g\sqrt{n_r}$, their hybridization becomes possible at increased photon number, see Fig. 3(c-f). The early breakdown of the dispersive approximation for $i_t^\star$ followed by the activation of near resonances is the cause of the observed bunching of the branch population at $N_t \sim i_t^\star$. This process starts with states closest to $i_t^\star$ and, pair by pair, is followed by states connected by multiphoton transition and that are symmetric about $i_t^\star$. This phenomenology explains why branch bunching, and thus ionization, typically occurs at lower photon number for the transmon's excited than the ground state, see Fig. 3(a). It also explains why, at moderate detuning, ionization typically occurs at much lower photon number for positive detuning than for negative detuning.

Figure 3(g) shows the average population of the branches when starting in $|\overline{1_t, 0_r}\rangle$ and evolving using Eq. (3). Around $\langle \hat{N}_r \rangle(t) \approx 7$, which coincides with branches 1_t and 7_t bunching around $N_r \approx 7$ in Fig. 3(a), a fraction of the population is transferred from branch 1_t to 7_t. However, even at the relatively high speed at which the resonance is traversed, most of the population remains in branch 1_t due to the wideness of the avoided crossing. The resonator population drops after the crossing due to drive becoming significantly off-resonant with the pulled resonator frequency associated with the ionized state.

In Ref. [7], this physics was shown to be captured within a semiclassical model in the RWA. In the full quantum model we use here, this can be understood by projecting the qubit-resonator Hamiltonian $\hat{H}_0$ of Eq. (1) on a subspace with N excitations. After a RWA, dropping n_g from the coupling term, and moving to a frame rotating at ω_r for the qubit and the resonator, this leads to

$$\begin{aligned}\hat{H}_0^N = &\sum_{i_t+n_r=N} (\omega_{i_t} - i_t\omega_r)\,|i_t, n_r\rangle\,\langle i_t, n_r| \\ &- ig_{i_t+1,i_t}\sqrt{n_r}\,|i_t+1, n_r\rangle\,\langle i_t, n_r - 1| + \mathrm{h.c.}\end{aligned} \tag{9}$$

This is analogous to a 1D lattice with nearest-neighbor hopping amplitude $g_{i_t+1,i_t}\sqrt{n_r}$. The bare energies of the sites $|i_t, n_r\rangle$ on this lattice form an inverted parabola with $|i_t^\star, N - i_t^\star\rangle$ at the top, see Fig. 4(a) [7]. For the parameters of Fig. 3, the states $|3_t, N-3_t\rangle$, $|4_t, N-4_t\rangle$, and $|5_t, N-5_t\rangle$ near the top of the parabola are near-degenerate and are connected by a single lattice hop. They therefore rapidly hybridize leading to the almost immediate state bunching seen at low photon number in Fig. 3(a). Hybridization between the other pairs of near degenerate states located on each side of the lattice becomes relevant once the photon number has increased enough to make the hopping amplitude sufficiently large

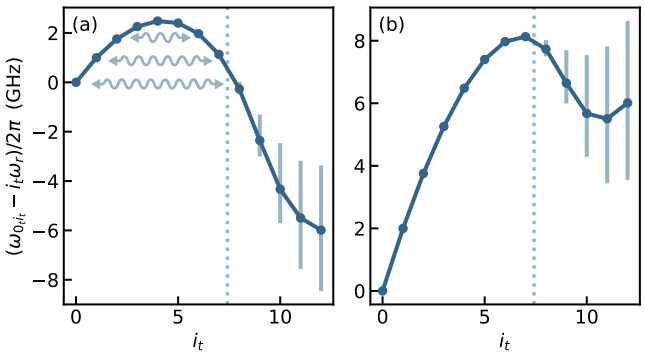

FIG. 4. **Positive detuning.** Bare energy $\omega_{0_t i_t} - i_t\omega_r$ of the sites $|i_t, N - i_t\rangle$ in the N-excitation subspace of $\hat{H}_0$ in the RWA illustrated for $N = 12$. (a) Parameters are as in Fig. 3 with $g = 0$ and $n_g = 0.25$. The site $|4_t, N - 4_t\rangle$ sits at the top of the inverted parabola. The arrows represent multiphoton processes connecting near-degenerate sites at the two extremities of the lattice. The full vertical lines represent the charge dispersion of level i_t. The dashed vertical line at $2E_J/\omega_p \sim 7.4$ indicates a lower bound for the number of states in the cosine potential well. Here, $\omega_p = \sqrt{8E_C E_J}$ is the plasma frequency. (b) Same parameters except for the larger positive detuning $\Delta/2\pi = 1.998\,\text{GHz}$ ($\omega_r/2\pi = 4.3\,\text{GHz}$).

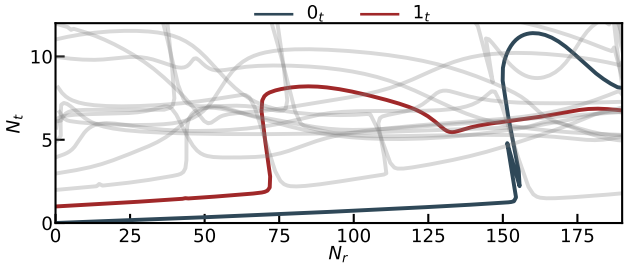

FIG. 5. **Positive detuning.** Average transmon population versus N_r for a larger positive detuning $\Delta/2\pi = 1.998\,\text{GHz}$ corresponding to $i_t^\star = 8$. Branches 0_t and 1_t are highlighted in color, the others are gray.

to allow virtual transitions between those two remote states. At that point, the wavefunctions of that pair of states become delocalized along the 1D lattice, and they join the layer of bunched states. This occurs pair by pair until the photon number is large enough for the ground state sitting at the bottom of the cosine potential well to finally enter the bunching layer together with its partner state, see Fig. 3(a).

This 1D model, however, is not sufficient to explain the situation at larger positive detuning, compare Fig. 3(a) to Fig. 5 obtained for $\Delta/2\pi = 1.998\,\text{GHz}$ ($\omega_r/2\pi = 4.3\,\text{GHz}$). The discrepancy is easily understood. Indeed, because the index $i_t^\star$ of the transmon level sitting at the top of the inverted parabola increases with the detuning, at large detuning states $i_t < i_t^\star$ no longer have quasidegenerate partners on the lattice, see Fig. 4(b). The absence of these multiphoton resonances tends to push ionization to larger photon numbers.

Moreover, at small resonator frequency with respect to the qubit frequency, more than N photons may be needed to connect pairs of states $|i_t, n_r\rangle$ associated to transmon states deep in the well to states near the top of the well. Considering only the projection on the N-excitation subspace is therefore no longer sufficient, signaling the breakdown of the RWA. More generally, Eq. (9) does not capture the full matrix elements of the transmon charge operator when states near or above the top of the cosine potential well are involved (see below).

As a result, while a bunching layer can still exist, at large positive detuning branch swapping associated with multiphoton transitions of the type discussed in Sec. II C is also observed. This is shown in Fig. 5 obtained for $\Delta/2\pi = 1.998\,\text{GHz}$, where this occurs for both the ground and excited branches. At large photon numbers, the increase with $\sqrt{n_r}$ of the coupling matrix elements is eventually sufficient to overcome the large energy separations. This leads to significant hybridization, causing the branches to merge with the bunching layer.

To summarize this section, the key ingredients leading to ionization at positive detuning are:

- Because of the transmon's negative anharmonicity, there generically exists a transmon state $i_t^\star$ for which the dispersive approximation breaks down at very low photon number. This results in rapid hybridization of the transmon states and to branch bunching close to $N_t \sim i_t^\star$.
- Branch bunching, and thus ionization, is precipitated by multiphoton resonances becoming relevant with the increase in photon number. This is captured within the RWA [7].
- At larger positive detuning, the RWA fails and weaker processes become dominant. As a result, multiphoton resonances involving the computational states are less likely. Generally, the photon number threshold for ionization increases with the detuning.

E. Gate-charge dependence

An important feature of the transmon is the exponentially small charge dispersion of its computational states with increasing E_J/E_C [2]. This charge dispersion, however, rapidly increases for states near and above the top of the cosine potential well, see the vertical full lines in Fig. 4. Because of the strong delocalization of the branches over the bare transmon states, see Fig. 3(c-f), even branches associated with states deep in the well exhibit charge sensitivity. As a result, the exact position of the resonances responsible for ionization depends on the gate charge. Moreover, these gate-charge sensitive states can be efficiently coupled to computational states given

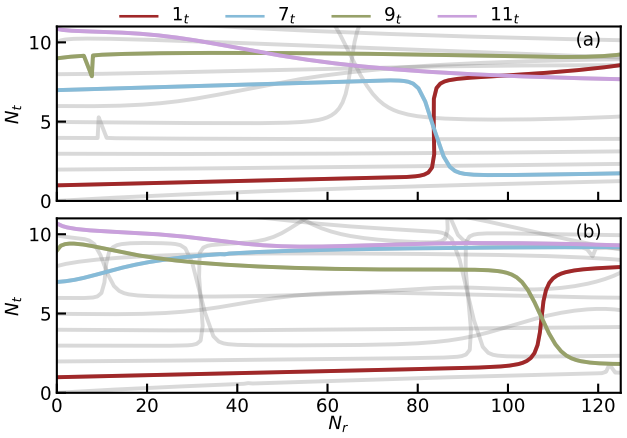

FIG. 6. **Negative detuning.** Average transmon population versus N_r for two different gates charge values (a) $n_g = 0$ and (b) $n_g = 0.3$. The parameters are the same as in Fig. 2. Branches B_{1_t}, B_{7_t}, B_{9_t} and B_{11_t} are highlighted (see legend), the others are gray. Ionization of the excited state is pushed back from $N_r \approx 84$ at $n_g = 0$ to $N_r \approx 108$ at $n_g = 0.3$.

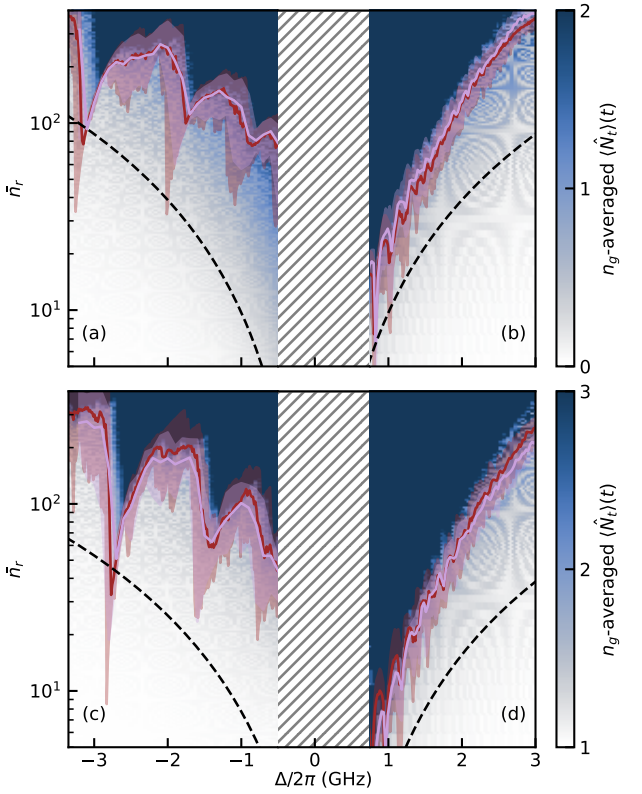

FIG. 7. Gate charge averaged critical photon number versus detuning extracted from the fully quantum model (pink), and Floquet analysis (red). The top panel corresponds to the ground state $\bar{n}^q_{\mathrm{crit},0_t}$ and $\bar{n}^f_{\mathrm{crit},0_t}$ for (a) negative detuning and (b) positive detuning. The bottom panel is for the qubit excited state $\bar{n}^q_{\mathrm{crit},1_t}$ and $\bar{n}^f_{\mathrm{crit},1_t}$ for (c) negative detuning and (d) positive detuning. Shaded areas correspond to the distribution of n^q_{crit,i_t} and n^f_{crit,i_t} between the 10th and 90th percentiles over 100 realizations of n_g for both models. The black dashed lines are the dispersive critical photon number n_{crit,i_t} defined in Appendix A for each state. The colored background shows the transmon population extracted from the gate charge averaged dynamics of a driven transmon, with steady-state photon number $\bar{n}_r(t \to \infty) = 400$, $\kappa/2\pi = 10\,\mathrm{MHz}$ (positive detuning) and $\kappa/2\pi = 1\,\mathrm{MHz}$ (negative detuning), see Sec. III for details. Note the change in color scale between the top and bottom panels.

that matrix elements such as $\langle i_t|\hat{n}_t|i_t + 3_t\rangle$ can be large. When moving away from the symmetry points $n_g = 0$ and 0.5, other matrix elements such as $\langle i_t|\hat{n}_t|i_t + 2_t\rangle$ also become large. Both the large charge dispersion and the influence of the gate charge on the matrix elements therefore significantly impacts the photon number at which ionization of the transmon computational states occurs, even deep in the transmon regime.

This is illustrated in Fig. 6 which shows the transmon branch population versus resonator photon number at negative detuning and for two values of the gate charge. For $n_g = 0$ (a), branches 7_t and 1_t form an avoided crossing at around $N_r \approx 84$ resulting in the observed branch swapping. In contrast, for $n_g = 0.3$ (b), because the charge operator can now connect states of the same parity, branch 11_t hybridizes early with 9_t and, in turn, branch 9_t hybridizes with 7_t. The result is a delayed ionization of 1_t at around $N_r \approx 108$. Dependence on gate charge is observed at positive detuning for the same reasons. The importance of gate charge on the driven transmon was also pointed out in Refs. [7, 21].

F. Critical photon number

Using the fully-quantum branch analysis, we now introduce critical photon numbers n^q_{crit,i_t} at which ionization of the transmon state i_t is expected to occur. These critical numbers are defined as the minimum photon number N_r at which the average transmon population reaches $N_t = 2$ for the ground state branch and $N_t = 3$ for the excited state branch. These choices capture large changes caused by resonances while avoiding to register the slow and smooth increase in N_t with photon number that is observed before ionization, see e.g. the red lines in Fig. 6. Given the sensitivity of ionization to gate charge, the critical photon numbers we report are averaged over 100 realizations of n_g between 0 and 0.5.

Figure 7 shows the resulting n_g-averaged critical photon number $\bar{n}^q_{\mathrm{crit},i_t}$ as a function of the qubit-resonator detuning (pink line). The top panels correspond to the ground state and the bottom panels to the excited state. We exclude a range of detunings around $\Delta = 0$ where the dispersive approximation does not hold (dashed region). The shaded pink area shows the distribution of $n^q_{\mathrm{crit},0_t}$ and $n^q_{\mathrm{crit},1_t}$ between the 10th and 90th percentiles for the

realization of n_g, emphasizing the strong dependence of ionization on gate charge. The usual Jaynes-Cummings critical photon number n_{crit,i_t} related to the breakdown of the dispersive approximation (see Appendix A) is shown as the black dashed line. Apart from a few values of n_g, the onset of ionization is well above n_{crit}. This observation is in agreement with Ref. [12] where a 99.1% dispersive readout fidelity was obtained at an average photon number $\bar{n}_r \sim 1.5 n_{\mathrm{crit}}$ larger than n_{crit}.

As a comparison, the background shows the average transmon population obtained from numerical integration of Schrödinger's equation for a driven transmon. We show in Sec. III how with the appropriate choice of time-dependent drive amplitude this simplified approach captures the essential physics of the full quantum model. Because of the strong dependence on n_g, the results are also averaged over 100 realization of the gate charge. The agreement between the critical photon numbers extracted from the branch analysis is excellent, confirming that the n^q_{crit,i_t} are useful and numerically simple to compute proxies for the onset of ionization.

The critical numbers n^q_{crit,i_t} exhibit a complex behavior as a function of detuning which can be understood from the phenomenology discussed in the previous sections. Focusing first on the case of negative detuning, we first observe the expected overall increase of n^q_{crit,i_t} with $|\Delta|$ due to the decrease of the χ_{i_t} shifts. As these shifts become smaller in magnitude, the slope of the modular energies decreases, pushing the energy collisions responsible for branch swapping to larger photon number and consequently increasing $n^q_{\mathrm{crit},0_t}$ and $n^q_{\mathrm{crit},1_t}$. On the other hand, the large detuning-dependent dips are due to branch swapping caused by anticrossings between the ground state [panel (a)] or excited state [panel (c)] branches with other branches. Increasing the detuning has the effect of sweeping through these resonances, resulting in the observed dips if the photon number at the anticrossing is large enough. For example, the three large dips in panel (a) result from resonances in the modular spectrum between the ground state branch and (from small to large negative detuning) branches B_{7_t}, B_{6_t} and B_{5_t}, see Appendix B for details.

At positive detuning, we also observe the expected overall increase of the critical photon numbers with detuning. On top of this behavior are sharp dips resulting from multiphoton resonances between the ground state [panel (b)] or excited state [panel (d)] and a quasiresonant partner state in the inverted potential of Fig. 4(a). At larger detuning, the ground and excited states no longer have a quasiresonant partner, see Fig. 4(b). As a result, this mechanism precipitating ionization is no longer active, and the increase of the critical photon number with detuning becomes more monotonic.

III. FLOQUET ANALYSIS OF THE DRIVEN TRANSMON

During qubit readout, the drive ε_d on the resonator displaces the resonator field to a coherent state with amplitude $\alpha(t)$ which, in turn, acts as a classical drive on the transmon [13, 27]. By making a displacement transformation $\hat{a} \to \hat{a} + \alpha(t)$ on the master equation, Eq. (3), and subsequently ignoring the quantum fluctuations of the resonator, we arrive at the simplified semiclassical picture of a driven transmon with Hamiltonian (see Appendix C)

$$\begin{aligned}\hat{H}(t) =& 4E_C(\hat{n}_t - n_g)^2 - E_J\cos(\hat{\varphi}_t) + \mathcal{E}_t(t)\hat{n}_t \\ =& \hat{H}_t + \mathcal{E}_t(t)\hat{n}_t.\end{aligned} \tag{10}$$

Assuming the resonator drive frequency ω_d to be close to the resonator frequency ω_r, the classical drive on the transmon is approximately $\mathcal{E}_t(t) \approx \varepsilon_t(t)\cos(\omega_d t)$, with a time-dependent amplitude $\varepsilon_t(t) = 2g\sqrt{\bar{n}_r(t)}$ where

$$\bar{n}_r(t) = \left(\frac{\varepsilon_d}{\kappa}\right)^2 (1 - e^{-\kappa t/2})^2 \tag{11}$$

is the average number of photons in the resonator, see Appendix C for details. In this model the resonator frequency ω_r of the full quantum model is replaced by the drive frequency ω_d. As a result, we place the qubit below or above ω_d when considering negative or positive detunings.

The effective drive on the transmon originates from the displacement of the transmon-resonator coupling and its amplitude is thus proportional to the coupling strength g. With the usual large values of g in circuit QED, this can lead to a very large effective drive amplitude on the transmon. For example, for the value $g/2\pi = 120\,\mathrm{MHz}$ used in this paper, we have $\varepsilon_t/2\pi \sim 750\,\mathrm{MHz}$ for $\bar{n}_r = 10$ photons in the resonator. This is significantly larger than the transmon anharmonicity α. Even though it is off resonant, this effective drive cannot be treated perturbatively and can be expected to lead to leakage out of the computational subspace. In this section, we show that this simplified model leads to the same predictions for transmon ionization as the full quantum model. The essence of the success of this simple approach is that it preserves the full cosine potential of the transmon qubit.

Because the effective drive amplitude $\varepsilon_t(t) \propto \sqrt{\bar{n}_r(t)}$ changes on a time scale $1/\kappa$ that is much larger than the period of the drive ($T = 2\pi/\omega_d$), our analysis relies on the instantaneous Floquet spectrum [28]. Considering $\hat{H}(t)$ to be periodic, in this approach the solution to Schrödinger's equation can be expressed as $|\psi(t)\rangle = \sum_{i_t} c_{i_t} e^{-i\epsilon_{i_t} t}|\phi_{i_t}(t)\rangle$ where ϵ_{i_t} is a Floquet quasienergy and $|\phi_{i_t}(t)\rangle = |\phi_{i_t}(t+T)\rangle$ a Floquet mode [29]. The phases $\exp(-i\epsilon_{i_t}T)$ and the Floquet modes $|\phi_{i_t}(t)\rangle$ are the eigenvalues and eigenvectors of the propagator over one period of the drive, $\hat{U}(t+T,t)|\phi_{i_t}(t)\rangle = e^{-i\epsilon_{i_t}T}|\phi_{i_t}(t)\rangle$. These eigenvalues

can also be obtained for a static Hamiltonian whose form is reminiscent of the transmon-resonator Hamiltonian, see Appendix D. Importantly, as the phases $\exp(-i\epsilon_{i_t}T)$ remain invariant under a shift of ϵ_{i_t} by an integer multiple of ω_d, the quasienergies ϵ_{i_t} are only defined modulo ω_d. Quasienergies are thus analogous to quasimomenta in Bloch theory and they are folded in a first 'Brillouin zone' $-\omega_d/2 \leq \epsilon_{i_t} \leq \omega_d/2$. Importantly, the Floquet modes and quasienergies are functions of the drive amplitude ε_t.

Just as in the previous section, we sort the Floquet quasienergies $\epsilon_{i_t}[\varepsilon_t]$ and modes $|\phi_{i_t}[\varepsilon_t]\rangle$ into transmon branches. Our labeling procedure at finite drive is performed by smoothly increasing the drive amplitude to connect the eigenstates of the unitary operator to those at zero drive. This is made possible by the fact that at zero drive, Floquet modes are simply the bare transmon eigenstates $|\phi_{i_t}[\varepsilon_t = 0]\rangle = |i_t\rangle$ and the quasienergies the bare transmon energies modulo the drive frequency $\epsilon_{i_t}[\varepsilon_t = 0] = E_{i_t} \mod \omega_d$. Given the above observations, the Floquet quasienergy spectrum is thus akin to the modular energy spectrum introduced above for the full quantum model. Both spectra capture changes in (quasi)energy with photon number and, thanks to the folding of the spectrum present in both cases, they can display avoided crossing between states corresponding to low- and high-energy transmon states, see e.g. Fig. 8(a). Avoided crossings in the quasienergy spectrum are thus linked to resonances between ac-Stark shifted transmon states, up to k drive photons of energy ω_d.

For unbounded Hamiltonians such as the transmon Hamiltonian, however, there are avoided crossings with quasienergy gaps of arbitrarily small sizes [30]. To avoid very small avoided crossings that are not relevant to transmon ionization, we numerically obtain the Floquet spectrum as a function of ε_t by setting a finite increment $\delta\varepsilon_t$ for tracking Floquet branches B_{i_t}. This contrasts with the branch construction of the full quantum model where, by default, one resonator photon is added at each step, corresponding to an increment $\sim g/\sqrt{n_r}$. Here, we take $\delta\varepsilon_t/2\pi = 10\,\text{MHz}$ which allows to capture the avoided crossing seen in the modular spectrum of the full quantum model. Another reason for this choice is that the effective drive amplitude $\varepsilon(t)$ is linked to the photon population of the resonator which in a qubit readout goes from 0 to a finite population $n_r(t)$ in a time scale set by κ. As such, the size of the increment $\delta\varepsilon_t$ can, to some extent, be linked to the system's dynamics. We have thus taken $\delta\varepsilon_t$ to be close to the value of $\kappa/2\pi = 7.95\,\text{MHz}$ used in our time-dependent simulations.

A. Negative detuning: $\omega_q < \omega_r$

We saw in Sec. II C that the opposite signs of the ac-Stark shifts of pairs of transmon branches (one deep in the cosine potential well and the other near the top of the well) results in avoided crossings in the modular energies. These avoided crossings — which can be precipitated by the early hybridization of states at the top of the well — result in transmon ionization during readout. We now show that the same phenomenology is present in the simplified model of the classically driven transmon, Eq. (10), with its full cosine potential.

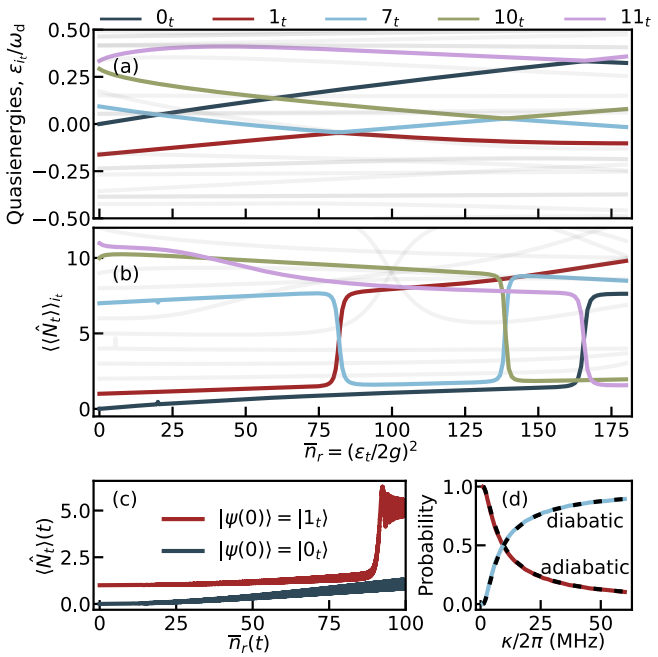

FIG. 8. **Negative detuning.** (a) Quasienergy spectrum and (b) period-averaged mean excitation number of the Floquet modes as a function of the mean resonator photon number $\bar{n}_r = (\varepsilon_t/2g)^2$ for a negative detuning $\Delta/2\pi = -1.217\,\text{GHz}$. Branches 0_t, 1_t, 7_t, 10_t and 11_t are highlighted in color (see legend), the others are gray. The transmon parameters are the same as in Fig. 2. (c) Time evolution of the mean number of excitation under a drive of amplitude $\varepsilon_t(t) = 2g\sqrt{100}(1 - e^{-\kappa t/2})$ with $\kappa/2\pi = 7.95\,\text{MHz}$ and frequency $\omega_d/2\pi = 7.515\,\text{GHz}$. The transmon is initialized in $|0_t\rangle$ (blue line) or $|1_t\rangle$ (red line). (d) Probability $|\langle\phi_{i_t}[\varepsilon_t(t_f)]|\hat{\mathcal{U}}(t_f)|1_t\rangle|^2$ of being in the Floquet mode $i_t = 1_t$ (red line, adiabatic) or $i_t = 7_t$ (light blue line, diabatic) vs. κ at the final time $t_f \approx 10/\kappa$ of the evolution. The dashed black lines are the Landau-Zener predictions, see Appendix E.

Figure 8(a) shows the numerically-obtained quasienergy spectrum as a function of the transmon drive amplitude here expressed in terms of the equivalent mean resonator photon number $\bar{n}_r = (\varepsilon_t/2g)^2$. The similarity with the modular energy spectrum of Fig. 2(b) obtained from the full quantum model is remarkable. In correspondence with Fig. 2(b), the quasienergies of states at the bottom and at the top of the cosine potential well move in opposite directions with $\bar{n}_r$ (see Appendix D), leading to avoided crossings at finite drive amplitudes. As an example, the quasienergies of branches 1_t (red line) and 7_t (light blue line) approach each other until an avoided crossing is formed at $\bar{n}_r \approx 82$ photons.

To illustrate the abrupt change in the character of the Floquet modes at the avoided crossings, we show in Fig. 8(b) the period-averaged transmon excitation,

$$\langle\langle \hat{N}_t \rangle\rangle_{i_t} = \frac{1}{T}\int_0^T d\tau \sum_{j_t} j_t |\langle j_t|\phi_{i_t}(\tau)\rangle|^2, \qquad (12)$$

for each Floquet branch as a function of $\bar{n}_r$. The similarity with the transmon population of the branches computed for the full transmon-resonator system of Fig. 2(a) is again remarkable, with branch swapping occurring at the resonances identified in Fig. 8(a). Note also the presence of small features at $\bar{n}_r \approx 22$ of the period-averaged transmon excitation corresponding to the branches 0_t (dark blue line) and 7_t (light blue line). This feature is due to a very small avoided crossing of the same two branches also at $\bar{n}_r \approx 22$, which, with our choice of increment $\delta\varepsilon_t$, is not resolved and is shown as a crossing, see Fig. 8(a). We confirm below that with our choice of κ this resonance does not play a role in the dynamics of the system.

To confirm that the observed resonances are responsible for transmon ionization in this semiclassical model, we now turn to time dynamics obtained under the Hamiltonian of Eq. (10) together with resonator decay κ, see Fig. 8(c). Here, ε_t is no longer a static control parameter but changes in time following $\varepsilon_t(t) = 2g\sqrt{\bar{n}_r(t)}$ with the average photon number given by Eq. (11). After preparing the transmon in the bare state $|\psi(0)\rangle = |i_t\rangle$ with $\varepsilon_t(0) = 0$, the state adiabatically follows the instantaneous Floquet mode of the i_t-th branch, $|\phi_{i_t}[\varepsilon_t(t)](t)\rangle$, as the drive amplitude is increased and until an avoided crossing with branch j_t is met. Following the usual Landau-Zener argument [29], at that point the state diabatically switches branch or adiabatically remains in the branch. This transition occurs with the Landau-Zener probability, $P_{\rm LZ} = \exp(-\pi\Delta_{\rm ac}^2/2v)$, where $\Delta_{\rm ac}$ is the quasienergy gap at the avoided crossing and $v(\varepsilon_t)$ the speed of passage through the resonance [31–34], see Appendix E. Importantly, ionization is averted if the state transitions diabatically through the crossing. By contrast, transitioning adiabatically means that the transmon ionizes.

In Fig. 8(c) we show a parametric plot of the transmon population as a function of time, here expressed in terms of $\bar{n}_r(t)$. When initially prepared in $|0_t\rangle$ (blue line), the state of the transmon follows branch 0_t, going straight through the weak avoided crossing at $\bar{n}_r \sim 22$ that our finite-step-size Floquet tracking purposely did not capture. In this case, the drive does not induce transitions in the transmon. On the other hand, when initially prepared in $|1_t\rangle$ (red line), the state follows mostly adiabatically branch 1_t through the avoided crossing at $\bar{n}_r \approx 82$ leading to a transition to high-energy transmon states. Figure 8(d) shows the probability of transitioning adiabatically or diabatically through the avoided crossing as a function of the rate at which $\varepsilon_t(t)$ varies. More precisely, we show as a function of κ [which controls $\varepsilon_t(t)$, see Eq. (11)] the probability of the state being in branch $i_t = 1_t$ (red line) or in branch $i_t = 7_t$ (light blue line) at the final time $t_f \approx 10/\kappa$ of the evolution. By increasing the value of κ and thus the speed at which resonances are crossed, the Landau-Zener probability for a diabatic crossing can be tuned from zero to almost one [20]. On top of these curves, we show the transition probability obtained from the Floquet-Landau-Zener formula (dashed black line) in perfect agreement with the time-dynamics simulations, see Appendix E.

The onset of ionization therefore depends on the effective speed at which resonances are crossed. According to Eq. (11), the drive ramp-up is faster at low photon numbers and slows down when approaching the steady-state photon number. We thus expect resonances that occur at the steady-state photon number to be more easily resolved. Consequently, ionization can be pushed back by driving the resonator stronger and thus diabatically crossing the resonance. This is observed experimentally in Ref. [6], wherein the probability of qubit ionization exhibits an initial rise at a certain drive power, followed by a subsequent decline at higher powers.

B. Positive detuning : $\omega_q > \omega_r$

Because of the negative anharmonicity of the transmon, the branch swapping observed at negative detuning is replaced by branch bunching at positive detuning. We now show that this phenomenology is captured by the simplified model of the classically driven transmon. Because ionization typically occurs at smaller resonator photon numbers at positive detuning than at negative detuning, larger discrepancies between the fully quantum model and the semiclassical model are expected.

Figure 9(a) and (b) shows the period-averaged transmon excitation of the Floquet branches and the quasienergy spectrum, respectively, versus $\bar{n}_r$ and obtained for the same parameters as in Sec. II D. Although there are some discrepancies especially at small photon numbers, the agreement with the modular spectrum of the full quantum model is nevertheless excellent, see Fig. 3. As in the full quantum model, rather than branch swapping we observe in Fig. 9(a) the expected branch bunching at $\langle\langle \hat{N}_t \rangle\rangle \sim 4$. The branch bunching also correctly correlates with anticrossings in the quasienergy spectrum. For example, at $\bar{n}_r \approx 6.4$, the quasienergies of branches 1_t and 7_t form a strong and wide avoided crossing, at which point we also observe the bunching of these two branches.

Interestingly, a weak avoided crossing of the quasienergies associated to 0_t and 8_t at $\bar{n}_r \approx 5.3$ is not captured with our finite tracking increment of $\delta\varepsilon_r/2\pi = 10\,\text{MHz}$. While the $1_t - 7_t$ transition requires the absorption of six drive photons, the $0_t - 8_t$ transition requires eight. It is hence more strongly suppressed and is not observed at this low drive amplitude. This higher-order transition, however, becomes relevant at larger drive amplitudes. In-

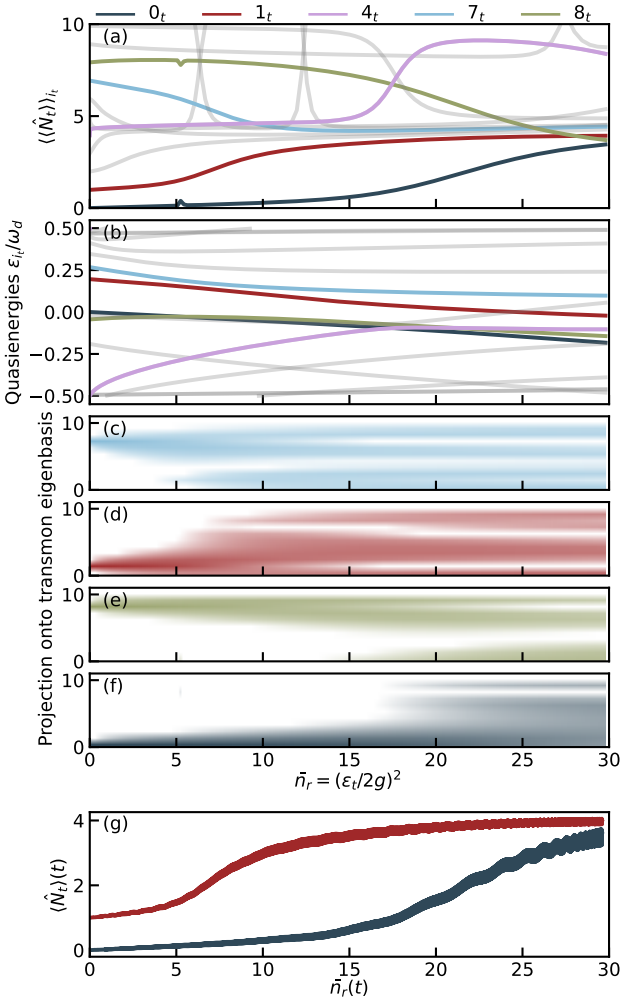

FIG. 9. **Positive detuning.** (a) Period-averaged mean excitation number of the Floquet modes, (b) Quasienergy spectrum, and (c)-(f) projection of the Floquet modes 7_t, 1_t, 8_t and 0_t on the transmon basis in logarithmic scale as a function of the mean resonator photon number $\bar{n}_r = (\varepsilon_t/2g)^2$ for a positive $\Delta/2\pi = 1.031\,\mathrm{GHz}$. In (a) and (b), branches 0_t, 1_t, 4_t, 7_t, and 8_t are highlighted in color (see legend), the others are gray. The transmon parameters are the same as in Fig. 3. (g) Time evolution of the mean number of transmon excitations under a drive of amplitude $\varepsilon_t(t) = 2g\sqrt{30}(1 - e^{-\kappa t/2})$ with $\kappa/2\pi = 11.98\,\mathrm{MHz}$ (set to match the full χ shift at zero photons), and frequency $\omega_d/2\pi = 5.267\,\mathrm{GHz}$. The transmon is initialized in $|0_t\rangle$ (blue line) or $|1_t\rangle$ (red line).

deed, at $\bar{n}_r \approx 18$ a weak level repulsion of the quasienergies associated to 0_t and 8_t are observed and which is correlated with the start of the bunching of these two states.

Those correlations are confirmed by the projection of the Floquet modes onto the bare transmon basis, see Fig. 9(c-f). There, we see that the Floquet modes associated to 0_t and 8_t show a strong delocalization in the transmon bare basis at $\bar{n}_r \approx 18$. On the other hand, for 1_t and 7_t this occurs at $\bar{n}_r \approx 6.5$, matching the presence of the avoided crossing in the quasienergy spectrum. To quantify the delocalization of the modes swallowed into the bunching layer, we compute the inverse participation ratio $\sum_{j_t} |\langle j_t|\phi_{i_t}\rangle|^4$ [35] which here measures the delocalization of a Floquet mode $|\phi_{i_t}\rangle$ on the transmon basis. At $\bar{n}_r \approx 11$, the inverse participation ratio is approximately $0.14 \approx 1/7$ for both $|\phi_{7_t}\rangle$ and $|\phi_{1_t}\rangle$, corresponding to a delocalization of these modes between at least seven transmon states.

To confirm that the presence of avoided crossings in the quasienergy spectrum is an accurate predictor of the system's dynamics, in Fig. 9(g) we show the time-dependent transmon population as a function of time, here parameterized by the instantaneous average photon number $\bar{n}_r(t)$. When the transmon is initialized in $|0_t\rangle$ (blue line), the state follows branch 0_t avoiding an early measurement-induced ionization at $\bar{n}_r \approx 5.3$. As a result, no feature is observed in $\langle\hat{N}_r\rangle(t)$ at that average photon number, except for a slow overall increase of the transmon population due to the gradual hybridization of branch 0_t. At $\bar{n}_r \approx 18$, the transmon population increases, as expected from the delocalization of that branch, see Fig. 9(f). On the other hand, when initialized in $|1_t\rangle$ (red line), the system mostly adiabatically transitions at the large avoided crossing at $\bar{n}_r \approx 6.4$, thereby following branch 1_t with a high probability. This results in measurement-induced transitions and to the observed rapid increase of $\langle\hat{N}_t\rangle(t)$.

C. Comparison to fully quantum model

We define the critical photon numbers in the Floquet analysis in a similar way as in the branch analysis of the fully quantum model. The Floquet critical photon numbers for the ground state $n^f_{\mathrm{crit},0_t}$ and for the excited state $n^f_{\mathrm{crit},1_t}$ are thus respectively defined as the smallest value of $\bar{n}_r$ for which $\langle\langle\hat{N}_t\rangle\rangle_{0_t} = 2$ and $\langle\langle\hat{N}_t\rangle\rangle_{1_t} = 3$. In Fig. 7, we compare the extracted n^f_{crit,i_t} (red line) with n^q_{crit,i_t} of the fully quantum model (pink line) for a range of detunings. The agreement between the two methods is excellent for both the average values and their fluctuations with charge noise (see the red and pink shaded areas). This agreement confirms the validity of treating the driven resonator as an effective classical field driving the transmon. Numerically, this approach is advantageous because of it simplicity and efficiency.

As previously mentioned, in Fig. 7 we also compare the critical photon numbers with the dynamics of the driven transmon (colored background). Because avoided crossings are very narrow in the negative detuning regime, we take a small $\kappa/2\pi = 1\,\mathrm{MHz}$ to ensure a slow ramp-up of the average photon number in the resonator. In this way, the system crosses slowy the resonances responsible for $\bar{n}^q_{\mathrm{crit},i_t}$ and $\bar{n}^f_{\mathrm{crit},i_t}$, leading to ionization in the time dynamics. At positive detunings, resonances are wider

and a faster ramp-up with $\kappa/2\pi = 10\,\mathrm{MHz}$ still results in ionization around $\bar{n}^q_{\mathrm{crit},i_t}$ and $\bar{n}^f_{\mathrm{crit},i_t}$. When comparing to experiments, the value of κ and ε_d used in the time-dynamical simulations can be adjusted to match the speed at which the resonator field builds up. For large speeds, early weak resonances will be crossed rapidly and therefore not lead to ionization. The step size $\delta\varepsilon_t$ in the Floquet tracking should be adjusted accordingly.

IV. NONLINEAR DYNAMICS OF A DRIVEN CLASSICAL TRANSMON

We have shown in Sec. III that a simplified model of a transmon driven by a classical monochromatic drive is enough to understand and predict the onset of ionization. In this section, we go one step further and investigate a model where the transmon itself is treated as a classical object. As in the previous sections, we account for the full nonlinearity of the transmon cosine potential and treat the readout drive nonperturbatively. This fully classical description, combined with the Bohr-Sommerfeld quantization rule, was shown in Ref. [21] to capture the main features of ionizing transitions. Here, we further clarify the classical mechanisms of ionization and explicitly connect them to the quantum phenomenology discussed in Sec. II and Sec. III.

A. General properties of the classical model

The full nonlinear dynamics of the classical transmon is governed by a dimensionless Hamiltonian that is formally identical to that of a driven classical pendulum [2]

$$\begin{aligned}\tilde{H}(\tilde{t}) &= \frac{1}{2}\tilde{n}_t^2 - \cos\tilde{\varphi}_t + \tilde{\varepsilon}_t\cos(\tilde{\omega}_d\tilde{t})\tilde{n}_t \\ &= \tilde{H}_t + \tilde{\varepsilon}_t\cos(\tilde{\omega}_d\tilde{t})\tilde{n}_t.\end{aligned} \tag{13}$$

Here, $\tilde{H}_t = H_t/E_J$ and $\tilde{t} = \omega_p t$ are rescaled energy and time, with $\omega_p = \sqrt{8E_JE_C}$ the transmon plasma frequency. Moreover, $\tilde{\varepsilon}_t = \varepsilon_t/\omega_p$, and $\tilde{\omega}_d = \omega_d/\omega_p$ are the rescaled transmon drive amplitude and drive frequency, respectively. The rescaled phase-space coordinates are $\tilde{\varphi}_t = \varphi_t$ and $\tilde{n}_t = zn_t$ with Poisson bracket $\{\tilde{\varphi}_t, \tilde{n}_t\} = z$, where $z = \sqrt{8E_C/E_J}$ is the transmon impedance [21]. We have omitted the gate charge n_g from Eq. (13) since a static gate charge does not affect classical dynamics. Moreover, as in Sec. III, the drive frequency ω_d is a surrogate for the resonator frequency of the full quantum model.

Given the periodic time dependence of Eq. (13), the solutions to Hamilton's equations are best studied using the Poincaré section obtained by plotting the phase-space coordinates stroboscopically at multiples of the drive period $\tilde{T} = 2\pi/\tilde{\omega}_d$. In Fig. 10, we show the Poincaré sections for a negative detuning (top panels) and for a positive detuning (bottom panels) of the drive to the qubit frequency. In each case, we show the Poincaré sections for increasing values of the drive amplitude $\tilde{\varepsilon}_t$. These results are obtained from the same values of the transmon parameters as above, here corresponding to $\omega_p/2\pi = 6.526\,\mathrm{GHz}$ and $z \sim 0.27$.

When $\tilde{\varepsilon}_t = 0$, two distinct types of regular orbits fill phase space, see panels (a) and (e). For $\tilde{H}_t < 1$, the system undergoes bounded periodic phase oscillations that are the classical analog of the transmon bound states. In the Poincaré section, these bounded oscillations correspond to the near circular orbits located in the center of phase space. Below, we will refer to these orbits as the main regular region. On the other hand, for $\tilde{H}_t > 1$ the system undergoes full $\pm 2\pi$ phase rotations, corresponding to phase slips in the quantum model [2]. This type of motion appears in the Poincaré section as nearly horizontal features that do not cross $\tilde{n}_t = 0$. Separating these two types of motion is the contour $\tilde{H}_t = 1$ known as the separatrix [olive line in Fig. 10(a,e)]. In the vicinity of the separatrix, small changes to the initial conditions can lead to large changes in the system's dynamics.

In addition to bounded and unbounded oscillations, for $\tilde{\varepsilon}_t > 0$ new types of motion are visible in the Poincaré sections. The first type of motion common to all panels of Fig. 10 where $\tilde{\varepsilon}_t > 0$ is chaotic motion. Chaos emerges in the vicinity of the separatrix for an arbitrarily weak drive amplitude and results from the instability of the system with respect to small perturbation at energies close to the separatrix. The size of the phase space region covered by chaotic motion generally increases with the drive amplitude [36, 37]. Critically, this process reduces the area of phase space supporting regular bounded oscillatory motion. This reduction of phase space area available to the main regular region due to the emergence of chaotic layers was identified as a key phenomenon responsible for the onset of ionization in the classical model [21].

The second type of motion seen in all panels of Fig. 10 for which $\tilde{\varepsilon}_t > 0$ is the presence of sets of islands surrounding the main regular region, see, e.g., the features highlighted in plum red, olive, and purple in panel (b) and the large croissant-shaped feature in panels (f,g,h). These features are subharmonic periodic orbits corresponding to $(n:m)$-nonlinear resonances occurring when $n\tilde{\omega}(\tilde{I}) = m\tilde{\omega}_d$ [36]. In this expression, $\tilde{\omega}(\tilde{I}) = \partial\tilde{H}_t/\partial\tilde{I}$, with $\tilde{I}$ the rescaled action variable, is the energy-dependent frequency of periodic motion of the pendulum which reduces to 1 at low energy. An $(n:m)$ resonance can be identified in phase space by a chain of n islands. We show below that in addition to the emergence of chaos the presence of these resonances is a second key phenomenon responsible for the onset of ionization within the classical model. Importantly, the phase-space area occupied by a resonance depends on n, with increasing values of n leading to smaller resonances, i.e., weaker resonances. The area occupied by a resonance and its distance from the center of the main regular region also generally depends on $\tilde{\varepsilon}_t$. As a result, although there is typically an abundance of $(n:m)$ resonances due to the

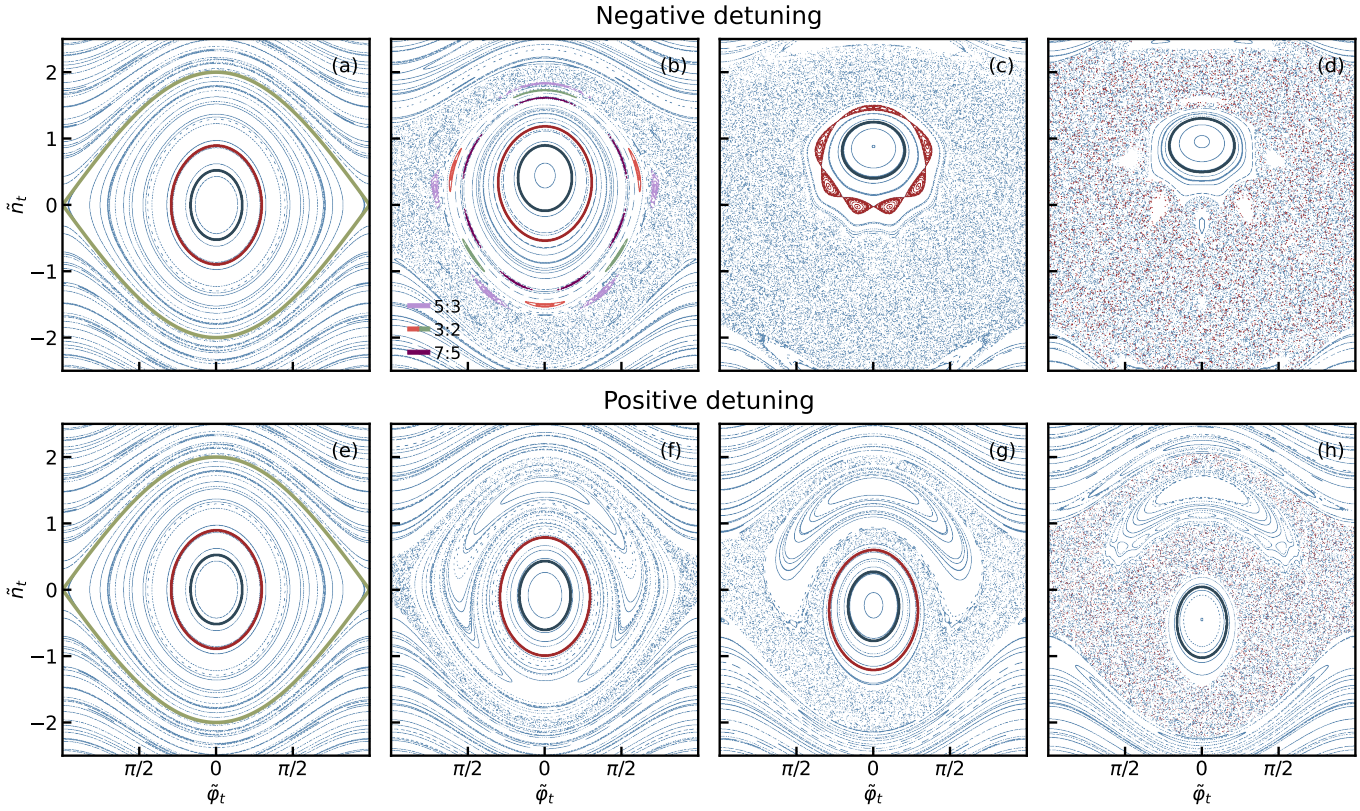

FIG. 10. Poincaré sections for different values of the drive amplitude $\tilde{\varepsilon}_t$ at negative (top row) and positive (bottom row) detunings. For negative detuning (a-d) the drive frequency is $\tilde{\omega}_d = 1.152$ ($\omega_d/2\pi = 7.515\,\mathrm{GHz}$, $\Delta/2\pi = -1.202\,\mathrm{GHz}$) and the drive amplitudes are, from left to right, $\tilde{\varepsilon}_t \in \{0, 0.167, 0.501, 0.624\}$ ($\bar{n}_r \in \{0, 20.6, 185.6, 287.6\}$). For positive detuning (e-h) the drive frequency is $\tilde{\omega}_d = 0.807$ ($\omega_d/2\pi = 5.267\,\mathrm{GHz}$, $\Delta/2\pi = 0.998\,\mathrm{GHz}$) and the drive amplitudes are, from left to right, $\tilde{\varepsilon}_t \in \{0, 0.029, 0.081, 0.152\}$ ($\bar{n}_r \in \{0, 0.63, 4.88, 17.02\}$). The Bohr-Sommerfeld orbits of the qubit ground and excited states are shown for $E_J/E_C = 110$ in dark blue and dark red, respectively. At zero drive amplitude, (a) and (e), the separatrix is shown in olive. In (b) (5:3) and (7:5) resonances are highlighted in purple and plum red, respectively. A pair of (3:2) resonances are also highlighted in orange and pale green. In (c) the (7:5) resonance collides with the Bohr-Sommerfeld orbit of the excited state. This is illustrated by coloring the resonance in red. In (d), merging of the excited state with the chaotic layer is assisted by a pair of (3:2) resonances that reduce the regular area available to the excited states. In (f-h) a (1:1) resonance occupies a large fraction of the region inside the main separatrix. At large drive amplitudes, (d) and (h), the excited state is engulfed by the chaotic layer. This is illustrated by the red points in the chaotic layer.

nonlinearity of $\tilde{\omega}(\tilde{I})$ [36], not all of those play an equally important role in ionization.

B. Bohr-Sommerfeld critical photon numbers

We now exploit the previous observations to predict the onset of ionization within the classical model. Interestingly, the relevance of chaotic behavior to the ionization of highly-excited Rydberg atoms was already pointed out [38–40]. Here, we follow Ref. [21] and use Bohr-Sommerfeld quantization to establish a correspondence between the strobsocopically obtained orbits in the Poincaré section and the Floquet modes of the transmon.

Since the rescaling of the dynamical coordinates in Eq. (13) does not preserve volumes in phase space, the quantization must proceed using an effective reduced Planck constant $\hbar_{\mathrm{eff}} = z = \sqrt{8E_C/E_J}$ [21]. The uncertainty principle then dictates that $2\pi\hbar_{\mathrm{eff}}$ is the area of phase space occupied by a single quantum state. As such, it imposes a limit to the resolution with which quantum states can probe the continuous structure of the classical phase space. While the classical limit is recovered by taking $\hbar_{\mathrm{eff}} \to 0$, we will see that classical dynamics remain a good predictor of ionization for large but finite values of E_J/E_C.

The quantized Bohr-Sommerfeld orbits for oscillatory motion are the classical orbits which enclose an area equal to [41]

$$\mathcal{A}_{i_t} = 2\pi\hbar_{\mathrm{eff}}\left(i_t + \frac{1}{2}\right), \tag{14}$$

where $i_t \in \{0, 1, 2, 3, \dots\}$ is the Bohr-Sommerfeld quantum number for the transmon. The number of Bohr-Sommerfeld states contained in a given area $\mathcal{A}$ of phase space is thus given by $\lfloor \mathcal{A}/2\pi\hbar_{\mathrm{eff}} \rfloor$. As an illustration,

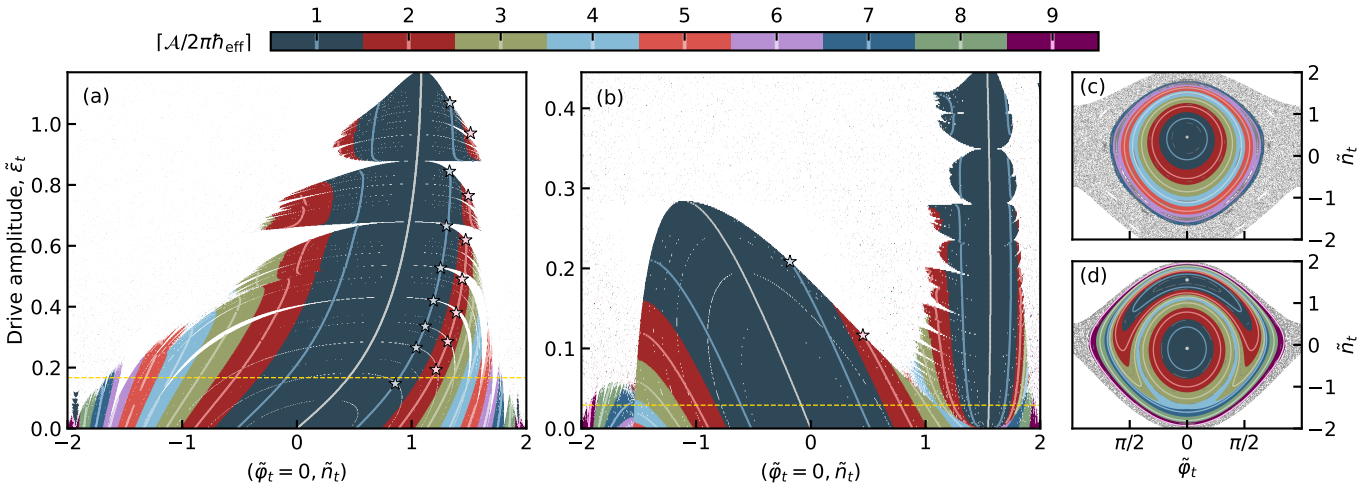

FIG. 11. Cut $(\tilde{\varphi}_t = 0, \tilde{n}_t)$ of phase space as a function of $\tilde{\varepsilon}_t$ for (a) negative detuning and ($\tilde{\omega}_d = 1.152$, $\omega_d/2\pi = 7.515\,\text{GHz}$, $\Delta/2\pi = -1.202\,\text{GHz}$) (b) positve detuning ($\tilde{\omega}_d = 0.807$, $\omega_d/2\pi = 5.267\,\text{GHz}$, $\Delta/2\pi = 0.998\,\text{GHz}$). The Bohr-Sommerfeld orbits are represented by pale colored lines and dark regions with matching colors quantum fluctuations of $\pi\hbar_{\rm eff}$ on each side of the Bohr-Sommerfeld orbits. The gray line centered at $\tilde{n}_t = 0$ at zero drive indicates the center of the main regular region, while the light blue and light red lines closest to it are the Bohr-Sommerfeld orbits of the qubit ground and excited states. In (b), the gray line at $\tilde{n}_t \approx 1.5$ indicates the center of the $(1:1)$ resonance. White regions indicate points where the algorithm of Appendix G fails to find a closed connected orbit due to chaotic or resonant motion. The points where the Bohr-Sommerfeld orbits of the qubit states stop existing (stars) yield the Bohr-Sommerfeld critical photon numbers $\{n^c_{\text{crit},i_t}\}$. As discussed in the text, weak resonances are ignored. Panels (c) and (d) show the Poincaré sections using the same color code corresponding to the drive amplitudes $\tilde{\varepsilon}_t = 0.167$ ($\bar{n}_r = 20.6$) and $\tilde{\varepsilon}_t = 0.029$ ($\bar{n}_r = 0.63$) indicated by the dashed yellow lines in panels (a) and (b), respectively. For $E_J/E_C = 110$ the effective Planck constant is $2\pi\hbar_{\rm eff} = 1.69445$. The horizontal axis scans initial conditions $(\tilde{\varphi}_t = 0, \tilde{n}^0_t)$ with $\tilde{n}^0_t \in [-2.0, 2.0]$ by increments of $1/300$. The vertical axis scans the drive amplitudes in increments of $\delta\tilde{\varepsilon}_t = 0.0015323$, corresponding to an increment of 10 MHz.

the orbits associated with the qubit ground and excited states are the blue and red orbits in Fig. 10. They are the orbits of the main regular region which enclose areas $\mathcal{A}_0 = \pi\hbar_{\rm eff}$ and $\mathcal{A}_1 = 3\hbar_{\rm eff}$, respectively. To account for quantum fluctuations, in our analysis we extend the area of Bohr-Sommerfeld states to include the area between $\mathcal{A}_{i_t} - \pi\hbar_{\rm eff}$ and $\mathcal{A}_{i_t} + \pi\hbar_{\rm eff}$. Note that because we are quantizing orbits obtained stroboscopically, the resulting Bohr-Sommerfeld orbits are the classical analog of the Floquet modes. We provide numerical evidence for this identification in Appendix F.

We expect the transmon drive to induce unwanted transitions for transmon state i_t whenever the Bohr-Sommerfeld orbit for that state cannot exist. Both chaotic dynamics and the presence of a $(n:m)$ resonance can prevent the existence of a given Bohr-Sommerfeld orbit. Indeed, the widening of the chaotic layer with increasing $\tilde{\varepsilon}_t$ reduces the number of Bohr-Sommerfeld orbits supported within the main regular region. In addition, a Bohr-Sommerfeld orbit can collide with a resonance for some values of $\tilde{\varepsilon}_t$. Moreover, as discussed further below, even a resonance appearing in the chaotic layer away from the qubit ground or excited orbits can facilitate ionization by reducing the regular area available to the qubit states.

Because it is difficult to visualize from Poincaré sections how features in phase space change with the drive amplitude, we instead plot in Fig. 11(a-b) a single cut $(\tilde{\varphi}_t = 0, \tilde{n}_t)$ of phase space as a function of $\tilde{\varepsilon}_t$. All three types of motions are easily identified on this figure. Focusing for the moment on panel (a), regular orbits correspond to the solid colored regions. The center of each Bohr-Sommerfeld orbits are represented as pale colored lines and the horizontal extent of the colored region about those lines accounts for quantum fluctuations. Notably, the blue and red regions correspond to the qubit ground and excited states, respectively. The chaotic layer appears as 'noise', and the nonlinear resonances as white gaps in the regular regions with wider gaps corresponding to stronger resonances.

At large enough drive amplitudes, all Bohr-Sommerfeld orbits are eventually absorbed by the chaotic layer and the colored regions disappear in the noise. This occurs earlier for orbits of large radius and last for the ground state orbit. Moreover, merging of the regular region with the chaotic layer is sometimes precipitated by resonances, e.g., see the large almost horizontal features close to $\tilde{\varepsilon}_t = 0.6$ and 0.9 in Fig. 11(a). Consequently, the regions where regular orbits exist often have a jagged shape reminiscent of a Christmas tree.

Another important observation is that the distance of resonances from the center of the main regular region goes down with the drive amplitude. As a result, resonances within the regular region collide with the Bohr-Sommerfeld orbits at some values of $\tilde{\varepsilon}_t$. For a given transmon state i_t, the values of $\bar{n}_r = (\omega_p/2g)^2\tilde{\varepsilon}_t^2$ at which the

center of the Bohr-Sommerfeld orbit i_t collides with a resonance or with the chaotic layer yield a set of critical photon numbers $\{n^c_{\mathrm{crit},i_t}\}$. These collisions are indicated by stars for 0_t and 1_t. Below, we assign an uncertainty on the value to those critical photons number by accounting for quantum fluctuations, i.e., the horizontal extent of the colored regions. Appendix G describes the systematic procedure that was used to build the Christmas trees, as well as to extract from them the values of $\{n^c_{\mathrm{crit},i_t}\}$ and of the lower bound that can be expected due to quantum fluctuations.

We now discuss how the above framework enables us to understand and predict ionization thresholds for the case of negative and positive detunings. In doing so, we connect this classical understanding to the quantum phenomenology described in the previous sections.

C. Negative detuning: $\omega_q < \omega_r$

We first consider the case of negative qubit-drive detuning, see Fig. 10(a-d). At any finite drive amplitude $\tilde{\varepsilon}_t$, a chaotic layer emerges in the vicinity of the separatrix of $\tilde{H}_t$, see panel (b) which is obtained at the small drive amplitude $\tilde{\varepsilon}_t = 0.167$ corresponding to $\bar{n}_r = 20.6$ photons. As a result, the area of the main regular region shrinks with increasing drive amplitude at the expense of the chaotic layer. Moreover, several nonlinear resonances can be identified in the chaotic or regular regions, and we have highlighted in color orbits associated with $(5:3)$, $(3:2)$, and $(7:5)$ resonances. At this drive amplitude, neither the chaotic layer nor the nonlinear resonances disrupt the orbits associated with the qubit logical states and we do not expect ionization to occur.

At larger drive amplitudes, the orbit of the nonlinear resonances in the regular region shrinks towards the center of the main regular region, see Fig. 11(a). At the drive amplitude corresponding to $\bar{n}_r = 185.6$, the $(7:5)$ resonance collides with the Bohr-Sommerfeld orbit associated with the qubit excited state, see Fig. 10(c) where the collision is illustrated by coloring the $(7:5)$ resonance in the color of the excited state. At that point, the qubit excited state can be unstable. Importantly, as discussed further below, this does not necessarily result in ionization. Indeed, weak resonances occupying a small area in phase space can cross the qubit states without damage. By further increasing the drive amplitude, the orbit of the resonance shrinks and no longer coincides with that of the qubit state. Given the abundance of nonlinear resonances, the pattern of resonances crossing and then moving away from the orbits of the qubit ground and excited states is a common occurrence. This is the reason for the jagged shape of the Christmas tree of Fig. 11(a) where large resonance lead to large windows of drive amplitude for which these orbits cannot exist. This observation is in agreement with the experimental results of Ref. [6] which showed that 'quiet spots' with minimal measurement-induced transitions could be found at average resonator photon number larger than the value where transitions are observed.

At a still larger drive amplitudes, initializing the classical system at the energy corresponding to the qubit excited states does not lead to a regular orbit but rather fills the chaotic layer, see Fig. 10(d) obtained for $\bar{n}_r = 287.6$. At that drive amplitude, the excited state is thus engulfed by the chaotic layer and is unstable. At yet larger drive amplitudes (not shown), the ground state eventually suffers the same fate and becomes unstable. It is interesting to note the presence in panel (d) of a pair of $(3:2)$ resonances near the inner edge of the chaotic layer. Because to each resonance is associated a new separatrix around which chaos emerges, the presence of those $(3:2)$ resonances further reduces the phase space available to the orbit associated with the qubit excited state, thereby hastening its merger with the chaotic layer. Note that the shrinking of the resonances towards the Bohr-Sommerfeld orbits associated with the qubit states is the classical analog of the quantum mechanism for ionization discussed in Sec. II C and Sec. III A, where high-energy states are ac Stark-shifted to lower energies until they hybridize with the qubit states.

Building on these observations, Fig. 12(a-b) shows the critical photon numbers $\{n^c_{\mathrm{crit},i_t}\}$ as a function of detuning Δ. The solid red lines indicate a collision of the orbit associated with the qubit (a) ground or (b) excited state with a resonance, while the hatched red lines rather indicate a collision with the chaotic layer. At $\Delta/2\pi = -1.202\,\mathrm{GHz}$ these lines correspond to the stars in Fig. 11(a). While chaos is expected to always induce ionization, this is not the case for all collisions with resonances. This is because many resonances occur at low photon numbers and are thus too weak to induce ionization. To account for this, the width of the solid red lines is proportional to the phase-space area of the resonance colliding with the qubit state orbit, which is in turn proportional to the resonance's strength. Using this information, the olive lines indicate the smallest critical photon number for which the phase-space area of the corresponding resonance is larger than $0.05 \times 2\pi\hbar_{\mathrm{eff}}$ in panel (a) and $0.10 \times 2\pi\hbar_{\mathrm{eff}}$ in panel (b). These values are free parameters and were chosen to best fit the classical model to the Floquet analysis, see the discussion below. The occasionally jagged behavior of that line in panel (a) occurs when the area of the relevant resonances becomes comparable to the resolution with which we compute phase-space areas.

These Bohr-Sommerfeld critical photon numbers are compared to the period-averaged transmon excitation $\langle\langle \hat{N}_t \rangle\rangle_{i_t}$ (colored background), a quantity which was shown to be a good indicator of transmon ionization in Sec. III. We have averaged the results over n_g to remove the dependence on this parameter. In both panels, we observe abrupt changes in $\langle\langle \hat{N}_t \rangle\rangle_{i_t}$ near the photon number where classical resonances occur. The agreement is excellent when discarding weak resonances which are not expected to have an effect on the qubit, see the olive

lines. That some resonances are not relevant to transmon ionization is consistent with the discussion in Sec. III A, where it was observed that weak resonances between Floquet modes do not cause ionization because they can be traversed diabatically. Other correspondences between the chaotic behavior of the driven classical pendulum and Floquet quasienergies are discussed in Ref. [21].

D. Positive detuning: $\omega_q > \omega_r$

We now turn to the case of positive detuning, see Fig. 10(e-h). As at negative detuning, a chaotic layer develops when the drive is made finite, see panel (f) obtained for $\bar{n}_r = 0.63$ photons. The most dramatic feature is, however, the appearance of a large $(1:1)$ resonance inside the separatrix of $\tilde{H}_t$. In Fig. 11(b), the domed-shaped feature centered at $\tilde{n}_t = 0$ at low amplitude correspond to the main regular region while the resonance is the Christmas tree-like feature centered at $\tilde{n}_t \sim 1.6$. This resonance results from the negative anharmonicity of the transmon which at positive detuning allows for $\tilde{\omega}(\tilde{I}) = \tilde{\omega}_d$ to be satisfied for some $\tilde{I}$. This is the classical equivalent of the breakdown of the dispersive approximation at zero photon number due to a 1-photon qubit-resonator resonance discussed in Sec. II D.

While this resonance typically does not collide with the Bohr-Sommerfeld orbit associated with the qubit ground and excited states, its presence rapidly restricts the phase space available to the main regular region. This is exacerbated by the presence of a new separatrix surrounding the $(1:1)$ resonance and about which a chaotic layer develops, see panel (g) obtained at $\bar{n}_r = 4.88$ photons and the V-shaped region between the main regular region and the resonance in Fig. 11(b). Increasing further the drive amplitude, the qubit excited state is engulfed by the chaotic layer and becomes unstable, see panel (h) obtained at $\bar{n}_r = 17.02$ photons. This is followed by the ground state also entering the chaotic layer at still larger photon number.

The area of the $(1:1)$ resonance is large enough ($> 2\pi\hbar_{\text{eff}}$) to support its own Bohr-Sommerfeld orbits, see Appendix F. In Fig. 11(b,d), these orbits share the same color code as the distinct orbits of the main regular region because they enclose the same areas. These orbits are located in phase space within the separatrix of $\tilde{H}_t$, and thus have an energy that is below the top of the cosine potential well of the transmon. This is in direct analogy with branch bunching about a state $i_t^\star$ located below the top of the well discussed in Sects. II D and III B. Moreover, additional $(n:m)$ resonances appear within the main regular region, see Fig. 11(b). However, these are small and are usually not relevant compared to the large $(1:1)$ resonance discussed above. Only at relatively large positive detunings does the critical photon number associated with the $(1:1)$ resonance become large enough to allow other $(n:m)$ resonances to become relevant for ionization (not shown).

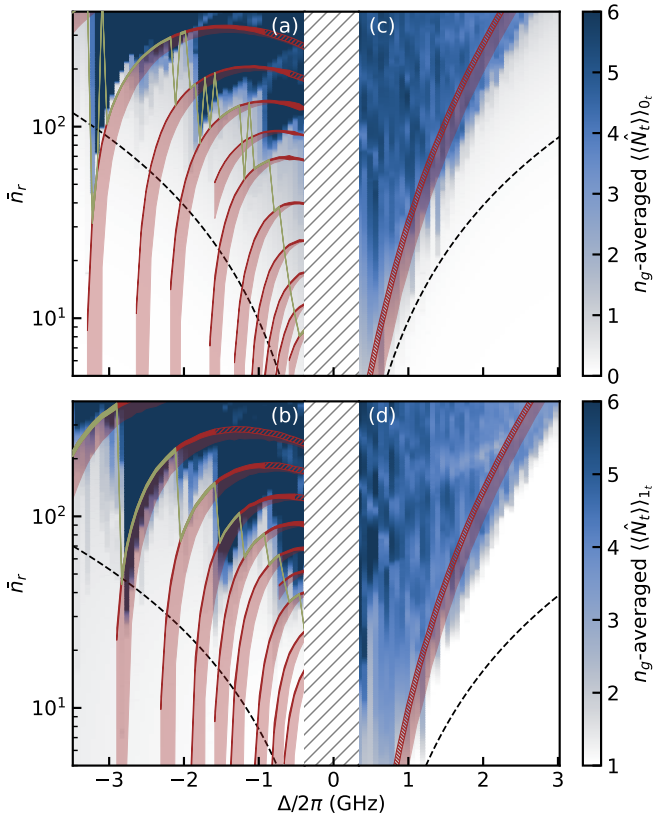

FIG. 12. Bohr-Sommerfeld critical photon numbers $\{n^c_{\text{crit},i_t}\}$ (red lines) and gate charge average of $\langle\langle\hat{N}_t\rangle\rangle_{i_t}$ (colored background) as a function of detuning Δ and photon number $\bar{n}_r$. The top panel corresponds to the qubit ground state for (a) negative detunings and (c) positive detunings, and the bottom panel for the qubit excited state for (b) negative detunings and (d) positive detunings. The hatched red lines indicate the critical photon numbers due to the chaotic layer while the solid red lines indicate the critical photon numbers due to a resonance. The width of the solid red lines is proportional to the phase-space area of the resonance while that of the hatched red lines was chosen to correspond to an area of $2\pi\hbar_{\text{eff}}$. The shaded red areas give the lower-bound uncertainty due to quantum fluctuations around the Bohr-Sommerfeld orbit. The black dashed lines are the standard Jaynes-Cummings critical photon number n_{crit,i_t} defined in Appendix A for each state. The hatched white regions indicate regions where the dispersive approximation does not hold and for which critical photon numbers were not calculated. In (a) and (b), the olive lines indicate the smallest critical photon number for which the phase-space area of the corresponding resonance is larger than $0.05 \times 2\pi\hbar_{\text{eff}}$ and $0.10 \times 2\pi\hbar_{\text{eff}}$, respectively. For both classical and Floquet theory, the vertical axis is produced by varying $\varepsilon_t/2\pi$ in increments of 10 MHz.

Fig. 12(c-d) shows the critical photon numbers $\{n^c_{\text{crit},i_t}\}$ as a function of positive detuning Δ and average photon number $\bar{n}_r$, with panel (c) corresponding to the ground state and panel (d) to the excited state. Because the small $(n:m)$ resonances crossing the qubit state orbits are of no consequences at this range of detun-

ing, the critical photon number here corresponds to the point where the qubit states are engulfed by the chaotic layer (hatched red lines). For most detunings, the presence of the large (1 : 1) resonance results in a much smaller critical photon number than at negative detuning. Also in contrast with the case of negative detuning, the Bohr-Sommerfeld critical photon number monotonically increases with the magnitude of the detuning since the (1:1) dominates the ionization mechanism.

The critical photon number is compared with the gate-charge average of $\langle\langle \hat{N}_t \rangle\rangle_{i_t}$ (colored background). Although the classical predictions tend to slightly overestimate the critical photon number obtained from Floquet theory, we again observe a good agreement between the two approaches over a large range of detunings and photon numbers. Some features that are not captured are the oscillations in the critical photon number at small detunings, see Fig. 13 for a clearer view of the oscillating features. As discussed in Sec. II D and Sec. III B, these arise from quantum tunneling physics and can thus not be captured within a classical model. In the broad strokes, however, the classical mode of the driven nonlinear pendulum captures remarkably well the essence of transmon ionization.

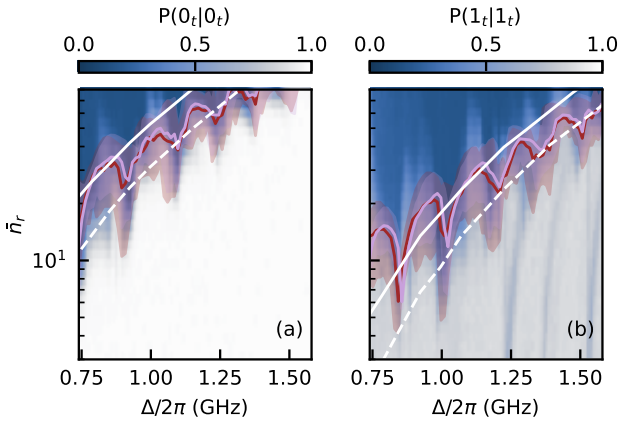

FIG. 13. Critical photon numbers of our three models compared to the experimental results of Ref. [7] for (a) ground state and (b) excited state. For a fixed detuning between the tunable transmon and resonator frequencies, the experiment consists of: preparing the transmon qubit in $|0_t\rangle$ or $|1_t\rangle$, driving the resonator at the conditional dressed frequency $\omega_{r,0_t}$ and $\omega_{r,1_t}$ and populating it with $\bar{n}_r$ photons on average, waiting for the resonator to decay back to the vacuum, and finally reading out the qubit to extract the conditional probabilities $P(i_t|i_t)$ of finding the outcome i_t given that $|i_t\rangle$ was initially prepared. The heat maps correspond to the experimental results. The red line shows our prediction of $\bar{n}^q_{\mathrm{crit},i_t}$ using the branch analysis of the full transmon-resonator system as explained in previous sections. The pink line shows $\bar{n}^f_{\mathrm{crit},i_t}$ obtained from the Floquet branch analysis. Shaded areas correspond to the distribution of n^q_{crit,i_t} and n^f_{crit,i_t} between the 10th and 90th percentiles over 100 realization of n_g. Finally, the white full line shows the prediction from the classical dynamics, with a lower bound given by white dashed line. The long vertical features in panel (b) at very low photon number and $\Delta/2\pi \gtrsim 1.25\,\mathrm{GHz}$ are attributed to the presence of two-level defects [7].

V. COMPARISON TO EXPERIMENTAL RESULTS

We now compare the critical photon numbers extracted from the quantum transmon-resonator, Floquet, and classical models to experimental data from Ref. [7]. This experiment consists in preparing the qubit in its ground or first excited states, filling the resonator with $\bar{n}_r$ photons for a controlled amount of time, and then performing a QND readout of the qubit state. The colored background of Fig. 13 shows the conditional probability $P(i_t|i_t)$ for the qubit to be measured in the state it was prepared in as a function of detuning and average resonator photon number. Panel (a) is for the ground state and panel (b) for the excited state. A white background indicates that the interaction with the $\bar{n}_r$ photons did not cause qubit leakage, while a dark background indicates leakage. In both cases, sharp dips are observed as a function of detuning. In that experiment, the readout resonator has a bare frequency $\omega_r/2\pi = 4.75\,\mathrm{GHz}$, the coupling constant is $g/2\pi = 91\,\mathrm{MHz}$, the charging energy is $E_C/2\pi = 194\,\mathrm{MHz}$, and the qubit frequency $\omega_q/2\pi$ can be tuned from 5.5 GHz to 6.34 GHz. In all cases, this corresponds to the regime of positive detuning.

In Ref. [7], a semiclassical model predicting the position and amplitudes of these dips is presented. Here we compare the experimental results to the critical photon number obtained from our fully quantum transmon-resonator (pink line) and classically-driven transmon (red line) models. The agreement with experimental results is excellent for both models and qubit initial states. Notably, the theoretical values capture the full detuning dependence of the critical photon number including the presence of dips in $\bar{n}_r$. Notably, it not only captures the position of these dips but also their height and width. Those dips correspond to the multiphoton resonances which are expected to precipitate ionization at positive detuning, see Sec. II D. Considering the experiment's slow time scale relative to gate charge fluctuations, the red and pink shaded areas—marking the critical photon numbers' distribution from the 10th to 90th percentiles over 100 samples of n_g—emphasize the necessity of including gate charge in these predictions. Moreover, as expected from the discussion in the previous sections, ionization typically occurs earlier for the qubit excited state than the ground state. Because it predicts the full dependence of the ionization threshold with detuning, including regions where $\bar{n}_{\mathrm{crit},0_t}$ and $\bar{n}_{\mathrm{crit},1_t}$ are large in between resonances, the framework presented here could be exploited to maximize readout performance.

The prediction from the classical model (white full

lines) follows the general trend of critical photon numbers as a function of detuning. The white dashed lines are a lower bound to these predictions accounting for quantum fluctuations. Because the classical model does not capture the multiphoton resonances responsible for accelerating ionization, the classical predictions do not capture the dips in critical photon number versus detuning. Yet, it is remarkable that as long as the full cosine potential is accounted for, obtaining excellent estimates of the photon number threshold for ionization matching experimental results can be obtained simply by solving Hamilton's equations of motion.

VI. CONCLUSION AND OUTLOOK

We have introduced a comprehensive framework providing a unified physical picture of the origin of transmon ionization. Our study is based on three complementary levels of description of the qubit-resonator system used for dispersive qubit readout in circuit QED. A first approach treats the qubit and the resonator as coupled quantum systems. A second approach simplifies the situation by replacing the driven resonator by a classical drive acting directly on the transmon. A third approach considers an entirely classical problem. All three approaches have in common that they rely on the full cosine potential of the tranmon's Josephson junction. The first two descriptions identify multiphoton resonances as the mechanism responsible for ionization. The positions of these resonances can be easily located, and estimates of critical photon numbers can be efficiently obtained numerically with both methods leading to predictions which are in agreement with each other and with recent experimental results. Those approaches also highlight the strong dependence of the critical photon numbers on gate charge, even deep in the transmon regime. The third level of description provides a simple interpretation based on the motion of a classical driven pendulum and its chaotic behavior. Although this method misses some features captured by the quantum models, the critical photon numbers it predicts are in qualitative agreement with the quantum predictions and with experimental results. It is remarkable that classical dynamics of the driven transmon is sufficient to capture the physics of ionization.

Although we have used throughout this work fixed sets of parameters, we have verified that the conclusions we have reached remain general. While, e.g., the specific multiphoton resonances precipitating ionization may shift with changes in parameters, the dependence of the critical photon numbers $\bar{n}^q_{\mathrm{crit},i_t}$ and $\bar{n}^f_{\mathrm{crit},i_t}$ on detuning preserves the same features.

We hope that the analyses presented in this work will facilitate the experimental exploration of parameter regions wherein transmon ionization occurs at large photon numbers. For example, this could be done by exploiting regions of detunings located between multiphoton resonances where the critical photon number can be large. Furthermore, despite the reduced dispersive shift, the use of large qubit-resonator detunings as a readout strategy seems promising and has not yet been extensively investigated. The increase in critical photon number with increasing absolute detuning $|\Delta|$ (see, e.g., Fig. 7) indicates the potential of this approach for improving qubit readout. Recent experimental findings lend support to this hypothesis [42]. Moreover, because the speed at which resonances are traversed affects the probability of ionization occurring, optimizing the readout pulse shape with an understanding of the position of resonance could prove to be beneficial.

Beyond dispersive readout, many experiments in circuit QED contain the basic ingredients that are at the core of ionization, namely strong drives and weak anharmonicities. These include but are not limited to other types of qubits [43, 44], readout schemes [45, 46], parametric gates [47, 48], and quantum state stabilization [49–51]. The tools introduced in this work can easily be applied to these scenarios. These tools are simple to interpret, have an easy construction, are easy to implement, and are computationally efficient. We thus anticipate the framework introduced in this work to become an integral part of the theoretical analysis and support of current and future circuit QED experiments.

ACKNOWLEDGEMENTS

The authors are grateful to Ross Shillito for helpful discussions. This work is supported by a collaboration between the US DOE and other Agencies. This material is based upon work supported by the U.S. Department of Energy, Office of Science, National Quantum Information Science Research Centers, Quantum Systems Accelerator. Additional support is acknowledged from NSERC, the Canada First Research Excellence Fund, the Ministère de l'Économie et de l'Innovation du Québec, and Fonds de recherche du Québec - Nature et technologies.

Appendix A: Dispersive critical photon number

In the main text, we compared the various critical photon numbers defined in our work with the critical photon number n_{crit,i_t} that defines the dispersive limit. Here, we summarize how these dispersive critical photon numbers are calculated.

The commonly used Jaynes-Cummings critical photon number for the qubit transition is defined as $n_{\mathrm{crit}} = |(\omega_{0_t 1_t} - \omega_r)/2g_{0_t 1_t}|^2$ [1, 4]. This is the photon number for which the interaction term in Eq. (1) becomes resonant with the qubit transition. However, this definition is insufficient to capture the breakdown of the dispersive regime in a multilevel system like the transmon. It is instead necessary to define a critical photon number for every transition [52]. To do so, we simply transpose the

definition for the qubit transition to all other transitions,

$$n_{\mathrm{crit},k_t l_t} \equiv \left| \frac{\omega_{k_t l_t} - \omega_r}{2 g_{k_t l_t}} \right|^2 . \tag{A1}$$

Note that this definition naturally includes counter-rotating transitions as the case where $\omega_{k_t l_t} \sim -\omega_r$. We define the dispersive critical photon number for an initial transmon state $|i_t\rangle$ as the smallest of the $n_{\mathrm{crit},k_t l_t}$ that involves the initial state:

$$n_{\mathrm{crit},i_t} = \min_{k_t l_t} \{ n_{\mathrm{crit},k_t l_t} | k_t = i_t \text{ or } l_t = i_t \}. \tag{A2}$$

Due to the dipole-like selection rules of the transmon regime, the limiting transitions for the qubit states are always $0_t \leftrightarrow 1_t$ and $1_t \leftrightarrow 2_t$. As a result, $n_{\mathrm{crit},0_t}$ and $n_{\mathrm{crit},1_t}$ are essentially independent of the gate charge n_g. Equation (A1) gives similar predictions as other definitions of the state-dependent critical photon numbers for the transmon [1], but has the advantage of being applicable to any multilevel system.

Appendix B: Nonperturbative corrections to the branches at negative detuning

In Sec. II C we argued that nonperturbative corrections to the approximate eigenstates obtained via Schrieffer-Wolff perturbation theory $|\overline{i_t, n_r}\rangle \equiv e^{-\hat{S}} |i_t, n_r\rangle \approx |\overline{i_t, n_r}\rangle$ was ultimately the cause of branch swapping. Here we discuss at length the mechanism through which these nonperturbative corrections occur.

As an illustrative example, let us consider the swapping of B_{1_t} and B_{7_t} which occurs at roughly 84 photons, see Fig. 2. If we were only to consider the bare transmon energies, swapping between these branches would be unexpected. Indeed, even if one considers the possibility of a multiphoton process connecting such states, the detuning between them is still large $(E_{7_t} - E_{1_t} - 4\omega_r)/2\pi \approx 1.98\,\mathrm{GHz} \gg g/2\pi$. Moreover, the interaction cannot directly add or remove 4 photons from the resonator, and any such process that appears within perturbation theory should be small. It is thus at this stage not evident why the swapping should occur between these branches.

To address how the requisite term mediating this process arises, we must keep more terms in the infinite-order expansion than in Eq. (6). To that end, we recall that the standard approach [2, 53] dictates that by choosing

$$\hat{S} = -i(\hat{S}_t \hat{a}^\dagger + \hat{a} \hat{S}_t) \tag{B1}$$

with

$$\hat{S}_t = \sum_{i_t, j_t = 0}^{\infty} \frac{g_{i_t j_t}}{\omega_{i_t j_t} - \omega_r} |i_t\rangle\langle j_t| \tag{B2}$$

we obtain

$$\begin{aligned} e^{\hat{S}} \hat{H}_{tr} e^{-\hat{S}} = {} & \omega_r \hat{a}^\dagger \hat{a} + \hat{H}_t + \hat{a}^\dagger \hat{a} \sum_{i_t, j_t = 0}^{\infty} \chi_{i_t j_t} |i_t\rangle\langle j_t| \\ & + \left(\hat{a}^\dagger \hat{a}^\dagger \sum_{i_t, j_t = 0}^{\infty} \eta_{i_t j_t} |i_t\rangle\langle j_t| + \mathrm{h.c.} \right) + \sum_{i_t, j_t = 0}^{\infty} \Lambda_{i_t j_t} |i_t\rangle\langle j_t| \\ & + O(g^3), \end{aligned} \tag{B3}$$

where the matrix matrix elements are

$$\chi_{i_t j_t} = \sum_{k_t = 0}^{\infty} g_{i_t k_t} g_{k_t j_t} \left(\frac{\omega_{i_t k_t}}{\omega_r^2 - (\omega_{i_t k_t})^2} + \frac{\omega_{j_t k_t}}{\omega_r^2 - (\omega_{j_t k_t})^2} \right), \tag{B4}$$

$$\eta_{i_t j_t} = \frac{1}{2} \sum_{k_t = 0}^{\infty} g_{i_t k_t} g_{k_t j_t} \left(\frac{1}{\omega_r - \omega_{k_t j_t}} - \frac{1}{\omega_r + \omega_{k_t i_t}} \right), \tag{B5}$$

$$\Lambda_{i_t j_t} = -\frac{1}{2} \sum_{k_t = 0}^{\infty} g_{i_t k_t} g_{k_t j_t} \left(\frac{1}{\omega_r - \omega_{k_t j_t}} + \frac{1}{\omega_r - \omega_{k_t i_t}} \right), \tag{B6}$$

and we have dropped all terms of order g^3 and higher. Note that we use a different notation than that presented in Ref. [2]. We note that Xiao *et al.* [22] introduce a diagramatic approach to obtain high-order effective Hamiltonian for a driven transmon in the absence of a resonance.

By keeping the diagonal terms in Eq. (B3), we recover Eq. (6) and thus correctly obtain the dispersion to order g^2. A salient feature of Eq. (B3), however, is that to that same order in the coupling we have terms that create pairs of photons in the resonator $\hat{a}^\dagger \hat{a}^\dagger$. These terms can also cause transitions between any transmon states with an amplitude $\eta_{i_t j_t}$. If we were to explicitly keep track of terms to higher-order in g, we would similarly conclude that to fourth order there appears an analogous term $\hat{a}^\dagger \hat{a}^\dagger \hat{a}^\dagger \hat{a}^\dagger$. Nevertheless, it would seem that this term is irrelevant, considering that it is of fourth order in a nominally small parameter.

As we emphasize in the main text, however, in this new basis the partially-diagonalized eigenstates are ac-Stark shifted. At large enough photon number, the $\hat{a}^\dagger \hat{a}^\dagger \hat{a}^\dagger \hat{a}^\dagger$ term that appears in the new basis can couple dressed states which are nearly degenerate. If the condition

$$\frac{|\langle \overline{1_t, n_r + 4} | \hat{H}_{tr} | \overline{7_t, n_r} \rangle|}{\left| \langle \overline{7_t, n_r} | \hat{H}_{tr} | \overline{7_t, n_r} \rangle - \langle \overline{1_t, n_r + 4} | \hat{H}_{tr} | \overline{1_t, n_r + 4} \rangle \right|} \gg 1 \tag{B7}$$

is satisfied for some n_r, the eigenstates are a highly-entangled superposition of $|\overline{1_t, n_r + 4}\rangle$ and $|\overline{7_t, n_r}\rangle$ and there is an avoided crossing in the spectrum. Before this occurs, the branch analysis classifies $|\overline{1_t, n_r}\rangle \approx |\overline{1_t, n_r}\rangle$ and $|\overline{7_t, n_r}\rangle \approx |\overline{7_t, n_r}\rangle$, but after the crossing the characters of the states have been switched and we have $|\overline{1_t, n_r}\rangle \approx |\overline{7_t, n_r - 4}\rangle$ and $|\overline{7_t, n_r}\rangle \approx |\overline{1_t, n_r + 4}\rangle$.

We can confirm this interpretation to be valid by plotting the overlaps of the approximate eigenstates with the relevant numerically-obtained eigenstates as in Fig. 14. We go to one order higher in perturbation theory than in Eq. (B3) by defining

$$|\overset{\cdots}{i_t, n_r}\rangle \equiv e^{-\hat{S}} e^{-\hat{T}} |i_t, n_r\rangle, \tag{B8}$$

where $\hat{T}$ is proportional to g^2 chosen to eliminate the off-diagonal terms to that order in Eq. (B3). Its explicit form is simple to obtain and is merely an exercise in commutator algebra and thus we do not reproduce it here. At low photon number, we see that $|\langle \overline{1_t, n_r}|\, \overset{\cdots}{1_t, n_r}\rangle|^2 \approx |\langle \overline{7_t, n_r}|\, \overset{\cdots}{7_t, n_r}\rangle|^2 \approx 1$, indicating the validity of the dispersive approximation. Near 84 photons, we see these overlaps experience a sharp drop, after which they become effectively zero. Instead, the overlaps $|\langle \overline{1_t, n_r}|\, \overset{\cdots}{7_t, n_r - 4}\rangle|^2$ and $|\langle \overline{7_t, n_r}|\, \overset{\cdots}{1_t, n_r + 4}\rangle|^2$ rise and become finite, indicating branch swapping. This makes it clear that near these photon numbers, these two approximate eigenstates are strongly mixed and the condition of Eq. (B7) is satisfied. The fact that the overlaps do not remain close to unity on each side of the branch swapping is a consequence of using a finite-order expansion for the partially-dressed eigenstates. Indeed, such an expansion becomes less accurate at large n_r since the transmon-resonator interaction strength scales with photon number. They could be made arbitrarily close to unity before and after the crossing by going to even higher order in perturbation theory. At the crossing itself, however, the observed branch swapping is always nonperturbative in the coupling g.

We emphasize that we focused on B_{1_t} and B_{7_t} since the branch analysis had already identified that these two had swapped. Without the branch analysis, we would need to verify the resonance condition, Eq. (B7), for every pair of branches. Further, we would need to ensure that the perturbative energies $\langle \overset{\cdots}{i_t, n_r}|\hat{H}_{tr}|\overset{\cdots}{i_t, n_r}\rangle$ are accurate. At higher photon number, this means going to higher order in perturbation theory, a needlessly tedious task given that the branch analysis already contains this information.

Finally, let us stress that the order of the multiphoton process responsible for the swapping of the ground or excited state branch with any other can be diagnosed by considering the modular spectrum of the bare transmon states. For instance, here we knew that the four-photon process was responsible for the swapping of the seventh and first branch since $(E_{7_t} - E_{1_t} - 4\omega_r)/2\pi = 1.98\,\mathrm{GHz}$ was the smallest detuning between these transmon states and any other multiphoton process. The order of these multiphoton resonances thus changes with the detuning Δ. For instance, going from small to large negative detuning, the three peaks we see in the detuning sweep of Fig. 7(a) are a consequence of the multiphoton process of order 4, 3, and 2 between the ground state and branches B_{7_t}, B_{6_t} and B_{5_t}, respectively.

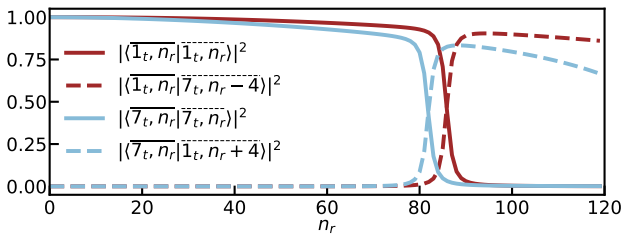

FIG. 14. Overlaps between the eigenstates of branches B_{1_t} and B_{7_t} and the corresponding perturbative approximations $|\overset{\cdots}{i_t, n_r}\rangle$ obtained via Schrieffer-Wolff perturbation theory, Eq. (B8). Before the branch swapping at approximately 84 photons, the eigenstates in each branch are well-approximated by their perturbative counterpart. Near the swapping, perturbation theory fails and the eigenstates are in a roughly equal superposition of the perturbative eigenstates. For larger photon number, the character of the eigenstates has switched. Deviation of the overlaps from unity beyond the swapping point is a consequence of the finite-order approximation for the $|\overset{\cdots}{i_t, n_r}\rangle$, which fails at large photon numbers.

Appendix C: Effective drive on the transmon

In Sec. III, we obtain Eq. (10) by applying a displacement transformation $\hat{D}(\alpha) = \exp(\alpha\hat{a}^\dagger - \alpha\hat{a})$ on the driven qubit-resonator master equation Eq. (3). In that transformation, the amplitude α is time dependent and takes the form $\alpha(t) = \int_0^t d\tau\, \mathcal{E}_d(\tau) e^{-(i\omega_r + \kappa/2)(t-\tau)}$. With that choice, the transformation eliminates the resonator drive from the Hamiltonian and induces an effective transmon drive $\mathcal{E}_t(t)\hat{n}_t = 2g\mathrm{Im}[\alpha(t)]\hat{n}_t$.

Taking the resonator drive to be $\mathcal{E}_d(t) = \varepsilon_d \sin(\omega_d t)$ with constant amplitude ε_d, we have that

$$\alpha(t) = \frac{\varepsilon_d}{2}\left[\frac{e^{-i\omega_d t} - e^{-(i\omega_r + \kappa/2)t}}{\omega_- - i\kappa/2} - \frac{e^{i\omega_d t} - e^{-(i\omega_r + \kappa/2)t}}{\omega_+ - i\kappa/2}\right], \tag{C1}$$

where $\omega_\pm = \omega_r \pm \omega_d$. The amplitude of the transmon drive therefore reads

$$\mathcal{E}_t(t) = g\varepsilon_d\left[\frac{\cos(\omega_d t - \phi_-) - \cos(\omega_r t - \phi_-)e^{-\kappa t/2}}{\sqrt{\omega_-^2 + (\kappa/2)^2}} - \frac{\cos(\omega_d t + \phi_+) - \cos(\omega_r t - \phi_+)e^{-\kappa t/2}}{\sqrt{\omega_+^2 + (\kappa/2)^2}}\right], \tag{C2}$$

where $\tan\phi_\pm = -2\omega_\pm/\kappa$. Because $\omega_+ \gg g\varepsilon_d$, we can ignore the second line of the above expression. Furthermore, assuming that $|\omega_-| \ll \kappa$, the drive amplitude takes the simpler form

$$\mathcal{E}_t(t) = \frac{2g\varepsilon_d}{\kappa}(1 - e^{-\kappa t/2})\cos(\omega_d t). \tag{C3}$$

This is the expression that we use in Sec. III.

Beyond this limiting regime, the effective drive on the transmon Eq. (C2) can still be well approximated by a fast periodic drive with an envelope that grows slowly as $(1-e^{-\kappa t/2})$, although not monotonically due to a finite difference $\omega_r-\omega_d$. In particular, for large $|\omega_r-\omega_d|$ compared to κ, an avoided crossing in the Floquet spectrum might be dynamically crossed multiple times.

An important remark is that, when $|\omega_r-\omega_d|\gtrsim\kappa$, a better approximation to the full transmon-resonator dynamics is still obtained by using Eq. (C3) rather than Eq. (C2) for just a driven transmon. The reason is that the resonator responds at a qubit-state-dependent frequency that is typically closer to the readout frequency ω_d than to ω_r, thus the monochromatic-tone approximation is more accurate.

Appendix D: Floquet formalism

While for the numerical simulations we extract the Floquet Hamiltonian directly from the evolution operator over one period, $\hat{U}(T)\equiv e^{-i\hat{H}_F T}$, it is instructive to express the Floquet problem in Shirley space, also known as the infinite replicas picture [54].

The replicas picture is obtained by solving the time-dependent Schrödinger equation in frequency space. Defining the Floquet quasienergies and modes of the time-dependent periodic Floquet Hamiltonian via $\hat{H}_F\left|\phi_{i_t}\right\rangle=\epsilon_{i_t}\left|\phi_{i_t}\right\rangle$, a particular solution to the Schrödinger equation is the Floquet state $\left|\psi_{i_t}(t)\right\rangle=e^{-i\epsilon_{i_t}t}\left|\phi_{i_t}(t)\right\rangle$. The quasienergy is defined within the first Brillouin zone $\epsilon_{i_t}\in[-\omega_d/2,\omega_d/2]$. The Floquet modes are periodic in time, $\left|\phi_{i_t}(t)\right\rangle=\left|\phi_{i_t}(t+T)\right\rangle$, where $\left|\phi_{i_t}(t)\right\rangle=\hat{U}(t)e^{it\hat{H}_F}\left|\phi_{i_t}(0)\right\rangle$ and $\left|\phi_{i_t}\right\rangle\equiv\left|\phi_{i_t}(0)\right\rangle$.

In the case of the driven transmon, expanding the Hamiltonian $\hat{H}_t(t)$ of Eq. (10) and the Floquet modes in Fourier components as $\hat{H}_t(t)=\hat{H}_t+(\varepsilon_t/2)(e^{i\omega_d t}+e^{-i\omega_d t})\hat{n}_t$ and $\left|\phi_{i_t}(t)\right\rangle=\sum_m e^{im\omega_d t}\left|\phi_{i,m}\right\rangle$ and substituting them in Schröginger's equation $i\partial_t\left|\psi_t(t)\right\rangle=\hat{H}(t)\left|\psi_t(t)\right\rangle$, leads to the eigenvalue problem

$$\begin{aligned}&(\hat{H}_t+m\omega_d)\left|\phi_{i_t,m}\right\rangle+\frac{\varepsilon_t}{2}\hat{n}_t(\left|\phi_{i_t,m+1}\right\rangle+\left|\phi_{i_t,m-1}\right\rangle)\\&=\epsilon_{i_t}\left|\phi_{i_t,m}\right\rangle.\end{aligned}\tag{D1}$$

The infinite replicas eigenvalue problem written in Eq. (D1) can be interpreted more clearly if written in matrix form as

$$\begin{aligned}&\begin{pmatrix}\ddots&\ddots&\ddots&&&\\\ddots&\hat{H}_t-\omega_d&\frac{\varepsilon_t}{2}\hat{n}_t&0&&\\\ddots&\frac{\varepsilon_t}{2}\hat{n}_t&\hat{H}_t&\frac{\varepsilon_t}{2}\hat{n}_t&\ddots&\\&0&\frac{\varepsilon_t}{2}\hat{n}_t&\hat{H}_t+\omega_d&\frac{\varepsilon_t}{2}\hat{n}_t&\\&&\ddots&\ddots&\ddots&\ddots\end{pmatrix}\begin{pmatrix}\vdots\\\left|\phi_{i_t,-1}\right\rangle\\\left|\phi_{i_t,0}\right\rangle\\\left|\phi_{i_t,1}\right\rangle\\\vdots\end{pmatrix}\\&=\epsilon_{i_t}\begin{pmatrix}\vdots\\\left|\phi_{i_t,-1}\right\rangle\\\left|\phi_{i_t,0}\right\rangle\\\left|\phi_{i_t,1}\right\rangle\\\vdots\end{pmatrix}.\end{aligned}\tag{D2}$$

The original time-dependent eigenvalue problem has thus been mapped to a static eigenvalue problem involving infinite replicas of transmons ordered in a one-dimensional lattice. The transmon at site m has a static Hamiltonian $\hat{H}_t+m\omega_d$ and is coupled to nearest neighbors $(m\pm1)$ sites via the operator $(\varepsilon_t/2)\hat{n}_t$. From that point of view, this "tunneling" operator couples transmon states belonging to neighboring replica sites. In the absence of a drive $\varepsilon_t=0$, the Floquet mode's component m is just $\left|\phi_{i_t,m}[\varepsilon_t=0]\right\rangle=\left|i_t,m\right\rangle$, i.e., the bare transmon state i_t at site m. Moreover, in the replicas picture, the bare states $\left|i_t,m\right\rangle$ and $\left|j_t,n\right\rangle$ can *hybridize* at finite ε_t provided that these states can be connected via a tunneling path along the one-dimensional lattice. Moving back to the original time-dependent picture, the interpretation is that there can be a transition between levels i_t and j_t provided $n-m$ drive photons at frequency ω_d are absorbed $(n>m)$ or emitted $(n<m)$.

With a second-order perturbative expansion in ε_t, we can compute a correction to the bare $(\varepsilon_t=0)$ frequencies $E_{i_t}+m\omega_d$. The ac Stark shift of level i_t is

$$\begin{aligned}\chi_{i_t,m}=&\frac{\varepsilon_t^2}{4}\sum_{j_t}\left(\frac{|\left\langle i_t\right|\hat{n}_t\left|j_t\right\rangle|^2}{E_{i_t,m}-E_{j_t,m+1}}+\frac{|\left\langle i_t\right|\hat{n}_t\left|j_t\right\rangle|^2}{E_{i_t,m}-E_{j_t,m-1}}\right)\\=&\frac{\varepsilon_t^2}{2}\sum_{j_t}\frac{\omega_{i_tj_t}|\left\langle i_t\right|\hat{n}_t\left|j_t\right\rangle|^2}{\omega_d^2-\omega_{i_tj_t}^2}\\=&2\bar{n}_r\sum_{j_t}\frac{\omega_{i_tj_t}|g_{i_tj_t}|^2}{\omega_d^2-\omega_{i_tj_t}^2},\end{aligned}\tag{D3}$$

where we have used the definitions $\omega_{i_tj_t}=E_{j_t}-E_{i_t}$, $g_{i_tj_t}=g\left\langle i_t\right|\hat{n}_t\left|j_t\right\rangle$, and $\varepsilon_t=2g\sqrt{\bar{n}_r}$. Note that this $\chi_{i_t,m}$ shift is independent of the replica index m, as expected as all replicas are equivalent. Importantly, this expression is exactly the frequency shift of the transmon level i_t with an average number of photons $\bar{n}_r$ in the resonator and for $\omega_d=\omega_r$ that is expected from Eq. (7) obtained with the full quantum model.

Appendix E: Floquet-Landau-Zener transition probability

The Landau-Zener formula for the transition probability at an anticrossing between two Floquet quasienergies gives accurate predictions, even for fast pulses [31, 34]. In our mapping of the driven transmon-resonator Hamiltonian to a Floquet problem, we do not directly change the detuning of the quasienergies linearly in time as would be the case for the standard Landau-Zener argument. Instead, the relevant parameters are the amplitude of the drive on the resonator ε_d and the resonator decay rate κ, which in turn changes the effective drive amplitude on the transmon following Eq. (C3). The latter is the quantity which controls the detuning between the quasienergies.

To deduce the effective speed v at which resonances are traversed as a function of the drive amplitude $\varepsilon_t(t)$, we follow Ref. [34] in approximating the difference in the quasienergies close to the avoided crossing as

$$\begin{aligned}\epsilon_{j_t}[\varepsilon_t(t)] - \epsilon_{i_t}[\varepsilon_t(t)] &\approx \sqrt{\Delta_{\rm ac}^2 + [v(t-t_{\rm ac})]^2} \\ &\approx \Delta_{\rm ac} + \frac{1}{2}\frac{[v(t-t_{\rm ac})]^2}{\Delta_{\rm ac}}.\end{aligned} \tag{E1}$$

In this expression, $t_{\rm ac}$ is the time at which the minimum gap $\Delta_{\rm ac}$ in the avoided crossing is reached. The value of the drive amplitude at that time is denoted $\varepsilon_{t,\rm ac} \equiv \varepsilon_t(t_{\rm ac})$. Expanding the left-hand-side of Eq. (E1) to second order (the first derivatives vanish at the avoided crossing), we obtain

$$\begin{aligned}&\epsilon_{j_t}[\varepsilon_t(t)] - \epsilon_{i_t}[\varepsilon_t(t)] \approx \epsilon_{j_t}[\varepsilon_{t,\rm ac}] - \epsilon_{i_t}[\varepsilon_{t,\rm ac}] \\ &+ \left|\frac{d^2\epsilon_{j_t}[\varepsilon_t]}{d\varepsilon_t^2}\right|_{\varepsilon_{t,\rm ac}} \left(\left.\frac{d\varepsilon_t(t)}{dt}\right|_{t_{\rm ac}}\right)^2 (t-t_{\rm ac})^2.\end{aligned} \tag{E2}$$

Combining the two above expressions, we find that the speed v is given by the relation

$$\frac{v^2}{2\Delta_{\rm ac}} = \left|\frac{d^2\epsilon_{j_t}[\varepsilon_t]}{d\varepsilon_t^2}\right|_{\varepsilon_{t,\rm ac}} \left(\left.\frac{d\varepsilon_t(t)}{dt}\right|_{t_{\rm ac}}\right)^2. \tag{E3}$$

Note that we assumed here that the second derivatives of $\epsilon_{i_t}[\varepsilon_t]$ and $\epsilon_{j_t}[\varepsilon_t]$ are equal at the avoided crossing.

Knowing the gap size $\Delta_{\rm ac}$ and the speed v, the Landau-Zener diabatic transition probability can be computed as $P_{\rm LZ} = \exp[-\pi\Delta_{\rm ac}^2/2v]$. For the parameters used in Fig. 8(c), we obtain $P_{\rm LZ} = 0.35$ for the diabatic crossing, and $1 - P_{\rm LZ} = 0.65$ for the adiabatic crossing. The quasienergy gap and the speed are numerically obtained from the tracked quasienergies and the functional form of the drive amplitude $\varepsilon_t(t)$.

Appendix F: Comparison of the Bohr-Sommerfeld energies with Floquet theory

In this appendix, we show that the Bohr-Sommerfeld quantization procedure gives a sensible approximation to quantum theory for standard transmon parameters. This is done by comparing the results obtained from the Bohr-Sommerfeld quantization approach to the Floquet analysis developed in Sec. III for $n_g = 0$. More precisely, we compare the time-averaged transmon energy over the coordinates $\{\varphi_{i_t}(\tau), n_{i_t}(\tau)\}$ for the Bohr-Sommerfeld orbits,

$$\langle\langle H_t\rangle\rangle_{i_t} = \lim_{t\to\infty}\frac{1}{t}\int_0^t d\tau\, H_t\big(\varphi_{i_t}(\tau), n_{i_t}(\tau)\big), \tag{F1}$$

to the time-averaged energy of the Floquet modes [21],

$$\langle\langle \hat{H}_t\rangle\rangle_{i_t} = \frac{1}{T}\int_0^T d\tau\, \langle\phi_{i_t}(\tau)|\, \hat{H}_t\, |\phi_{i_t}(\tau)\rangle\,. \tag{F2}$$

In these plots, the gray symbols correspond to the Floquet modes energy given by Eq. (F2), the colored symbols to the time-averaged energies of the Bohr-Sommerfeld orbits given by Eq. (F1). For the latter, we use the same color code as in Fig. 11. The scale of the vertical axis is chosen such that zero energy corresponds to the bottom of the cosine well while $2E_J$ to the energy of the top of the well, i.e. the energy of the separatrix of H_t. The significance of the colored full and dashed lines will be explained below.

Focusing first on the case of negative detuning, we first observe that the average energy of the Floquet modes (gray symbols) located near the bottom of the well change smoothly with drive amplitude at small drive amplitude. On the other hand, modes located near the separatrix rapidly hybridize resulting in erratic behavior with the drive amplitude. In Ref. [21], this was shown to be a signature of chaotic behavior. As the drive amplitude is further increased, the chaotic layer widens until it absorbs the Floquet modes associated with the qubit logical states. Note that the resonances responsible for ionization can be seen as sharp features of the average energy connecting Floquet modes at the bottom of the well with modes close to the top of the well.

Before chaotic behavior emerges, the energy of the Bohr-Sommerfeld orbits (colored symbols) match very well the average Floquet energies. It is interesting to note that this is the case even in this situation where there are few levels in the well. The classical method is thus quite robust. Moreover, the discontinuities that are observed in the energies of the Bohr-Sommerfeld orbits coincide with the ranges of $\tilde{\varepsilon}_t$ for which the corresponding orbits cease to exist because of collisions with $(n:m)$ resonances. The full and dashed pink lines denote the average energies of the orbit at the center of the main regular region [corresponding to the gray line in Fig. 11(a)] and the average energy of the outermost orbit of the main regular region, respectively. These two lines delimit the energy window into which regular orbits exist, i.e., where Bohr-Sommerfeld states are supported. The correspondence between the pink dashed line and the region where the average Floquet energy shows chaotic behavior is striking.

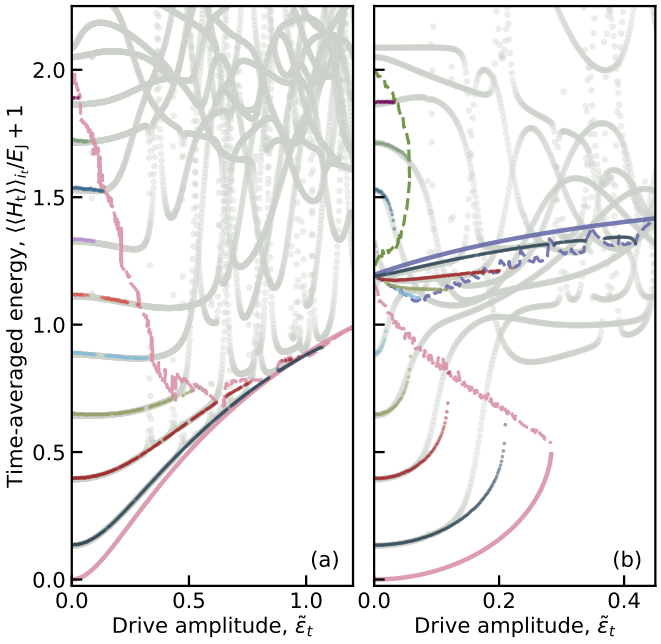

FIG. 15. Time-averaged energies $\langle\langle H_t\rangle\rangle_{i_t}$ of the Bohr-Sommerfeld orbits (colored dots with color code of Fig. 11) and time-averaged energies $\langle\langle \hat{H}_t\rangle\rangle_{i_t}$ of the Floquet modes at $n_g = 0$ (gray dots) as a function of the rescaled drive amplitude $\tilde{\varepsilon}_t$. The solid lines indicate the energies of the center of the main regular region (pink) and the $(1:1)$ resonance (indigo). The dashed lines indicate the energy of the boundaries of the regular regions, namely the main regular region (pink), the $(1:1)$ resonance (indigo), and the innermost and outermost orbits external to the $(1:1)$ resonance at positive detuning (green). We show (a) the case of negative detuning ($\tilde{\omega}_d = 1.152$) and (b) the case of positive detuning ($\tilde{\omega}_d = 0.807$). The Bohr-Sommerfeld $\langle\langle H_t\rangle\rangle_{i_t}$ are obtained by averaging the Hamiltonian over $\mathcal{N} = 1000$ periods using 40 points per period. The Floquet $\langle\langle \hat{H}_t\rangle\rangle_{i_t}$ are obtained using 31 points per period. The drive amplitude is varied in increments of $\delta\varepsilon_t/2\pi = \omega_p\delta\tilde{\varepsilon}_t/2\pi = 10\,\mathrm{MHz}$. The Bohr-Sommerfeld orbits and the region boundaries were identified using the procedure described in Appendix G.

At positive detunings we again see an excellent agreement between the classical and the Floquet predictions at small drive amplitudes, see Fig. 15(b). Notably, both approaches show the emergence of a set of states in the vicinity of $i_t = 4$ whose energy changes smoothly with drive amplitude. This is the bunching layer caused by a $(1:1)$ resonance discussed in Sec. II D and Sec. III B. Chaotic behavior emerges not only close to the separatrix of $\tilde{H}_t$ but also close to the bunching layer. This is the behavior expected from Figs. 10 and 11 and results from the apperance of a new separatix close to the resonance. Increasing further the drive amplitude, the chaotic layer widens until all states inside the cosine potential become chaotic.

Because of the presence of the large $(1:1)$ resonance, there are three different regions that can support Bohr-Sommerfeld states, namely the main regular region, the $(1:1)$ resonance itself, and the orbits surrounding both the main regular region and the $(1:1)$ resonance, see Fig. 11(b). In Fig. 15(b), the full and dashed pink lines correspond to the average energy of the orbits at the center and inner edge of the main regular region, respectively. Furthermore, the full and dashed indigo lines are the energy of the center and inner edge of the $(1:1)$ resonance. The lower and upper dashed green lines are the average energy of the innermost and outermost orbits external to the $(1:1)$ resonance. The agreement between the Bohr-Sommerfeld energies and Floquet modes energies in the three identified zones is excellent. We have verified that the correspondence between the bunching layer Floquet states and the $(1:1)$ resonance holds better as $\hbar_{\mathrm{eff}}$ is made smaller (not shown). In the limit $\hbar_{\mathrm{eff}} \to 0$ ($E_J/E_C \to \infty$), the lowest energy Bohr-Sommerfeld state coincides with the energy of the center of the main regular region and ionizes at around $\tilde{\varepsilon}_t \sim 0.3$ where the pink full and dashed lines meet in Fig. 15. Consequently, the Bohr-Sommerfeld critical photon number associated to the $(1:1)$ resonance has a saturating value.

Finally, we note that the center of the $(1:1)$ resonance is a point of stability with higher time-averaged energy than the surrounding points. Thus, the bunched states are excitations within an effective inverted potential well generated by the drive. Such an inverted effective potential well bears a superficial resemblance to the Kapitza pendulum, i.e. a rigid pendulum stabilized 'upside-down' by periodically changing the height of the pivot point. With the $(1:1)$ resonance of interested here, however, the stabilized orbits oscillate around $\varphi = 0$ and not around $\varphi = \pm\pi$.

Appendix G: Calculation of the Bohr-Sommerfeld critical photon numbers

In this appendix we describe the method used to compute the Bohr-Sommerfeld critical photon numbers $\{n^c_{\mathrm{crit},i_t}\}$ introduced in Sec. IV B. The key is to determine whether the Bohr-Sommerfeld orbit associated with a given qubit state i_t exists. If the orbit is chaotic or overlaps with a $(n:m)$ resonance, there exists no closed and fully connected regular orbit with the required area, and the qubit state is then declared unstable. The different photon numbers at which the Bohr-Sommerfeld orbit associated to qubit state i_t becomes nonexistent yield the Bohr-Sommerfeld critical photon numbers $\{n^c_{\mathrm{crit},i_t}\}$.

For a given value of the rescaled drive frequency $\tilde{\omega}_d$ (i.e., a fixed value of the detuning Δ) and of the rescaled drive amplitude $\tilde{\varepsilon}_t$, we solve Hamilton's equations to obtain the orbits over $\mathcal{N}$ drive periods corresponding to all initial conditions along the axis $(\tilde{\varphi}_t = 0, \tilde{n}^0_t)$, with $\tilde{n}^0_t \in [-2.0, 2.0]$ varied in increments of $1/300$. We then attempt to compute the area of all orbits using Green's theorem. More precisely, we choose some phase-space field $\mathbf{F} = \{P(\tilde{\varphi}_t, \tilde{n}_t), Q(\tilde{\varphi}_t, \tilde{n}_t)\}$ such that $\nabla \times \mathbf{F}$ is a unit vector perpendicular to the phase-space plane. With that

choice, Green's theorem yields

$$\begin{aligned}\mathcal{A} &= \iint_{\mathcal{D}} (\nabla \times \mathbf{F}) \cdot d\mathbf{A} = \oint_{\mathcal{C}} \mathbf{F} \cdot \mathbf{dr} \\ &\approx \sum_{\nu} \left[P(\tilde{\varphi}_t^{\nu}, \tilde{n}_t^{\nu}) \Delta\tilde{\varphi}_t^{\nu} + Q(\tilde{\varphi}_t^{\nu}, \tilde{n}_t^{\nu}) \Delta\tilde{n}_t^{\nu} \right],\end{aligned} \tag{G1}$$

where the sum is over all points ν in the orbit, and where $\Delta\tilde{\varphi}_t^{\nu} = \tilde{\varphi}_t^{\nu} - \tilde{\varphi}_t^{\nu-1}$ and $\Delta\tilde{n}_t^{\nu} = \tilde{n}_t^{\nu} - \tilde{n}_t^{\nu-1}$ are the coordinate differences between adjacent points of the orbit. A simple choice for $\mathbf{F}$ is $P(\tilde{\varphi}_t, \tilde{n}_t) = 0$ and $Q(\tilde{\varphi}_t, \tilde{n}_t) = \tilde{\varphi}_t$, yielding

$$\mathcal{A} \approx \left| \sum_{\nu} \tilde{\varphi}_t^{\nu} \Delta\tilde{n}_t^{\nu} \right|. \tag{G2}$$

The absolute value is present to obtain a positive area independently of the integration direction along the orbit. In general, the points of an orbit in the Poincaré section are not naturally ordered along the orbit because they are obtained stroboscopically. We must therefore order the points of an orbit to compute an area using Eq. (G2). If most points of an orbit can be ordered on a closed and connected near-continuous orbit, an area can be successfully calculated and a closed orbit with that area can exist. In all other cases, a closed connected orbit cannot exist.

In the attempt to order the points along an orbit, we start at the initial point of the orbit. We then find the point in the Poincaré section that is closest to the initial point in phase space. The nearest neighbor of this second point is then selected, excluding the points that were already selected. The procedure is repeated until it returns to the initial point or until the nearest neighbor is farther than a threshold distance d chosen as

$$d = \begin{cases} \frac{2\pi r_c m}{\mathcal{N}} & \text{if} \quad \frac{\mathcal{N} d_{\min}}{2\pi m} < r_c < \frac{\mathcal{N} d_{\max}}{2\pi m}, \\ d_{\min} & \text{if} \quad r_c \leq \frac{\mathcal{N} d_{\min}}{2\pi m}, \\ d_{\max} & \text{if} \quad r_c \geq \frac{\mathcal{N} d_{\max}}{2\pi m} \text{ or no main region.} \end{cases} \tag{G3}$$

Here, m is a scalar and r_c is the distance between the initial condition $(0, \tilde{n}_t^0)$ and the center of the main regular region (determined as described below). The first condition in Eq. (G3) sets the distance threshold in proportion to the expected average distance between orbit points. Indeed, the quantity $2\pi r_c/\mathcal{N}$ is the average arc length between orbit points distributed uniformly on a circle of radius r_c. Thus, m is the number of average arc lengths tolerated between nearest neighbors. The second and third conditions in Eq. (G3) set a minimum and maximum distance between nearest neighbors, respectively. The minimum distance $d_{\min}$ ensures that the threshold d remains finite very close to the center of the main regular region, although such small orbits are not relevant for the parameter regime explored in this work provided that the area corresponding to a circle of radius $\mathcal{N} d_{\min}/2\pi m$ is smaller than the smallest area a Bohr-Sommerfeld orbit can enclose, namely $\mathcal{A}_0$. The maximal distance $d_{\max}$ ensures that the threshold remains finite far from the main regular region or when the main regular region stops existing. This mitigates the number of chaotic orbits for which the algorithm occasionally finds a closed connected orbit (these appear as "noise" in the white regions of Fig. 11). The algorithm records a successful area calculation if it returns to the initial point and if the number of ordered points is larger than $\mathcal{N}/2$ and otherwise records a failure. The latter condition prevents identifying a single island of a disconnected subharmonic resonant orbit as a closed connected orbit. For the above procedure, we used $\mathcal{N} = 1000$, $2\pi m/\mathcal{N} \approx 0.65$, $d_{\min} = 0.10$ and $d_{\max} = 0.80$, which gave us fast and reliable results.

Setting the threshold d using Eq. (G3) requires knowledge of the position of the center of the main regular region at all drive amplitudes. At $\tilde{\varepsilon}_t = 0$, the center sits at $(0, 0)$ in phase space. If the drive amplitude is slightly increased, the center slightly moves away from its former position such that an orbit with initial condition $(0, 0)$ now encloses the new center. The position of the new center is estimated as the center of mass of that orbit. The method is iterated until the main regular region stops existing. This is detected by the orbit wandering too far away from the previous center position. To track the center, we increment $\tilde{\varepsilon}_t$ by 0.01, use orbits with $\mathcal{N} = 1500$ periods, and set the wandering off threshold distance to 1.0. In Fig. 11, the center of the main regular region is shown as gray lines starting at $(0, 0)$ at zero drive amplitude in panels (a-b) while it appears as gray dots in panels (c-d).

The above procedure allows us to compute the phase-space area of orbits as a function of $\tilde{\omega}_d$ and $\tilde{\varepsilon}_t$. We first vary $\tilde{\omega}_d$ [Δ] between 0.5 [3.02 GHz] and 1.5 [-3.49 GHz] in increments of 0.01, but exclude very small detunings $\tilde{\omega}_d \in (0.90, 1.03)$ [$\Delta \in (-0.47, 0.41)$ GHz] where the dispersive approximation is not expected to hold. For each value of $\tilde{\omega}_d$, we then vary $\tilde{\varepsilon}_t$ in increments of $\delta\tilde{\varepsilon}_t = \delta\varepsilon_t/\omega_p = 0.0015323$, corresponding to $\delta\varepsilon_t/2\pi = 10$ MHz. The results are shown in Fig. 11 for a fixed value of a (a) negative detuning and (b) positive detuning. The colored regions indicate the initial conditions where an area was successfully calculated. In particular, the Bohr-Sommerfeld orbits are highlighted as pale lines. The dark colored regions represent the extent of quantum fluctuations around a given Bohr-Sommerfeld orbit. More precisely, they contain all orbits with an area within $\pi\hbar_{\text{eff}}$ of that orbit at fixed $\tilde{\varepsilon}_t$. The white regions indicate the initial conditions where the algorithm failed to calculate an area. The Bohr-Sommerfeld critical photon numbers $\{n^c_{\text{crit},i_t}\}$ are the points when the Bohr-Sommerfeld line for state i_t collides with the white regions as the drive amplitude is increased. These points are represented by stars in Fig. 11. A lower bound to the $\{n^c_{\text{crit},i_t}\}$ from quantum fluctuations is obtained from the points where the boundaries of the dark colored regions collide with the white regions as the drive amplitude is increased. These points are not shown in Fig. 11.

Finally, we quantify the strength of the resonances at the critical photon numbers by the area they occupy in phase space, see Fig. 12 of the main text. To obtain the area of a resonance, we start at a critical point in Fig. 11 (star). We then vary $\tilde{n}_t^0$ across the resonance at fixed $\tilde{\varepsilon}_t$. The area of the resonance is then obtained as the difference of the areas of the two orbits that jointly enclose the resonance. We repeat this procedure for every relevant resonance.

[1] Alexandre Blais, Arne L. Grimsmo, S. M. Girvin, and Andreas Wallraff, "Circuit quantum electrodynamics," Rev. Mod. Phys. **93**, 025005 (2021).

[2] Jens Koch, Terri M. Yu, Jay Gambetta, A. A. Houck, D. I. Schuster, J. Majer, Alexandre Blais, M. H. Devoret, S. M. Girvin, and R. J. Schoelkopf, "Charge-insensitive qubit design derived from the Cooper pair box," Phys. Rev. A **76**, 042319 (2007).

[3] A. Wallraff, D. I. Schuster, A. Blais, L. Frunzio, J. Majer, M. H. Devoret, S. M. Girvin, and R. J. Schoelkopf, "Approaching unit visibility for control of a superconducting qubit with dispersive readout," Phys. Rev. Lett. **95**, 060501 (2005).

[4] Alexandre Blais, Ren-Shou Huang, Andreas Wallraff, S. M. Girvin, and R. J. Schoelkopf, "Cavity quantum electrodynamics for superconducting electrical circuits: An architecture for quantum computation," Phys. Rev. A **69**, 062320 (2004).

[5] T Walter, P Kurpiers, S Gasparinetti, P Magnard, A Potočnik, Y Salathé, M Pechal, M Mondal, M Oppliger, C Eichler, and A Wallraff, "Rapid high-fidelity single-shot dispersive readout of superconducting qubits," Phys. Rev. Appl. **7**, 054020 (2017).

[6] Daniel Sank, Zijun Chen, Mostafa Khezri, J. Kelly, R. Barends, B. Campbell, Y. Chen, B. Chiaro, A. Dunsworth, A. Fowler, E. Jeffrey, E. Lucero, A. Megrant, J. Mutus, M. Neeley, C. Neill, P. J. J. O'Malley, C. Quintana, P. Roushan, A. Vainsencher, T. White, J. Wenner, Alexander N. Korotkov, and John M. Martinis, "Measurement-induced state transitions in a superconducting qubit: Beyond the rotating wave approximation," Phys. Rev. Lett. **117**, 190503 (2016).

[7] Mostafa Khezri, Alex Opremcak, Zijun Chen, Kevin C. Miao, Matt McEwen, Andreas Bengtsson, Theodore White, Ofer Naaman, Daniel Sank, Alexander N. Korotkov, Yu Chen, and Vadim Smelyanskiy, "Measurement-induced state transitions in a superconducting qubit: Within the rotating-wave approximation," Phys. Rev. Appl. **20**, 054008 (2023).

[8] Z. K. Minev, S. O. Mundhada, S. Shankar, P. Reinhold, R. Gutiérrez-Jáuregui, R. J. Schoelkopf, M. Mirrahimi, H. J. Carmichael, and M. H. Devoret, "To catch and reverse a quantum jump mid-flight," Nature **570**, 200–204 (2019).

[9] François Swiadek, Ross Shillito, Paul Magnard, Ants Remm, Christoph Hellings, Nathan Lacroix, Quentin Ficheux, Dante Colao Zanuz, Graham J. Norris, Alexandre Blais, Sebastian Krinner, and Andreas Wallraff, "Enhancing dispersive readout of superconducting qubits through dynamic control of the dispersive shift: Experiment and theory," (2023), arXiv:2307.07765 [quant-ph].

[10] J. E. Johnson, C. Macklin, D. H. Slichter, R. Vijay, E. B. Weingarten, John Clarke, and I. Siddiqi, "Heralded state preparation in a superconducting qubit," Phys. Rev. Lett. **109**, 050506 (2012).

[11] S. Touzard, A. Kou, N. E. Frattini, V. V. Sivak, S. Puri, A. Grimm, L. Frunzio, S. Shankar, and M. H. Devoret, "Gated conditional displacement readout of superconducting qubits," Phys. Rev. Lett. **122**, 080502 (2019).

[12] Y. Sunada, S. Kono, J. Ilves, S. Tamate, T. Sugiyama, Y. Tabuchi, and Y. Nakamura, "Fast readout and reset of a superconducting qubit coupled to a resonator with an intrinsic Purcell filter," Phys. Rev. Appl. **17**, 044016 (2022).

[13] Cristóbal Lledó, Rémy Dassonneville, Adrien Moulinas, Joachim Cohen, Ross Shillito, Audrey Bienfait, Benjamin Huard, and Alexandre Blais, "Cloaking a qubit in a cavity," Nat. Commun. **14**, 6313 (2023).

[14] Liangyu Chen, Hang-Xi Li, Yong Lu, Christopher W. Warren, Christian J. Križan, Sandoko Kosen, Marcus Rommel, Shahnawaz Ahmed, Amr Osman, Janka Biznárová, Anita Fadavi Roudsari, Benjamin Lienhard, Marco Caputo, Kestutis Grigoras, Leif Grönberg, Joonas Govenius, Anton Frisk Kockum, Per Delsing, Jonas Bylander, and Giovanna Tancredi, "Transmon qubit readout fidelity at the threshold for quantum error correction without a quantum-limited amplifier," npj Quantum Inf. **9**, 26 (2023).

[15] Morten Kjaergaard, Mollie E. Schwartz, Jochen Braumüller, Philip Krantz, Joel I.-J. Wang, Simon Gustavsson, and William D. Oliver, "Superconducting qubits: Current state of play," Annu. Rev. Condens. Matter Phys. **11**, 369–395 (2020).

[16] Maxime Boissonneault, J. M. Gambetta, and Alexandre Blais, "Nonlinear dispersive regime of cavity QED: The dressed dephasing model," Phys. Rev. A **77**, 060305 (2008).

[17] Maxime Boissonneault, J. M. Gambetta, and Alexandre Blais, "Dispersive regime of circuit QED: Photon-dependent qubit dephasing and relaxation rates," Phys. Rev. A **79**, 013819 (2009).

[18] Alexandru Petrescu, Moein Malekakhlagh, and Hakan E. Türeci, "Lifetime renormalization of driven weakly anharmonic superconducting qubits. II. The readout problem," Phys. Rev. B **101**, 134510 (2020).

[19] Ryo Hanai, Alexander McDonald, and Aashish Clerk, "Intrinsic mechanisms for drive-dependent Purcell decay in superconducting quantum circuits," Phys. Rev. Res. **3**, 043228 (2021).

[20] Ross Shillito, Alexandru Petrescu, Joachim Cohen, Jackson Beall, Markus Hauru, Martin Ganahl, Adam G.M. Lewis, Guifre Vidal, and Alexandre Blais, "Dynamics of transmon ionization," Phys. Rev. Appl. **18**, 034031 (2022).

[21] Joachim Cohen, Alexandru Petrescu, Ross Shillito, and Alexandre Blais, "Reminiscence of classical chaos in driven transmons," PRX Quantum **4**, 020312 (2023).

[22] Xu Xiao, Jayameenakshi Venkatraman, Rodrigo G. Cortiñas, Shoumik Chowdhury, and Michel H. Devoret, "A diagrammatic method to compute the effective Hamiltonian of driven nonlinear oscillators," (2023), arXiv:2304.13656 [quant-ph].

[23] Maxime Boissonneault, J. M. Gambetta, and Alexandre Blais, "Improved superconducting qubit readout by qubit-induced nonlinearities," Phys. Rev. Lett. **105**, 100504 (2010).

[24] R. Shillito, *Simulation and Optimization of Superconducting Qubit Control and Readout*, Ph.D. thesis, Université de Sherbrooke (2023).

[25] Howard J Carmichael, *Statistical Methods in Quantum Optics 2* (Springer Berlin Heidelberg, 2007).

[26] Emitting and absorbing a virtual photon — corresponding to the first and second term in Eq. (7) respectively — leads to an oppositely-signed ac-Stark shift for the transitions of interest. The former processes are less detuned due to the negative anharmonicity and the corresponding contributions are larger in magnitude, leading to a positive slope χ_{i_t} for states at the bottom of the cosine potential. However $|g_{i_t j_t}|^2$ is larger for higher-excited states, and the virtual emission processes become dominant, leading to a negative χ_{i_t} for states at the top of the well.

[27] Manuel H. Muñoz Arias, Cristóbal Lledó, and Alexandre Blais, "Qubit readout enabled by qubit cloaking," Phys. Rev. Appl. **20**, 054013 (2023).

[28] H.P. Breuer and M. Holthaus, "Quantum phases and Landau-Zener transitions in oscillating fields," Phys. Lett. A **140**, 507–512 (1989).

[29] Milena Grifoni and Peter Hänggi, "Driven quantum tunneling," Phys. Rep. **304**, 229 – 354 (1998).

[30] Daniel W. Hone, Roland Ketzmerick, and Walter Kohn, "Time-dependent Floquet theory and absence of an adiabatic limit," Phys. Rev. A **56**, 4045–4054 (1997).

[31] K. Drese and M. Holthaus, "Floquet theory for short laser pulses," Eur. Phys. J. D **5**, 119–134 (1999).

[32] William D. Oliver, Yang Yu, Janice C. Lee, Karl K. Berggren, Leonid S. Levitov, and Terry P. Orlando, "Mach-Zehnder interferometry in a strongly driven superconducting qubit," Science **310**, 1653–1657 (2005).

[33] S.N. Shevchenko, S. Ashhab, and Franco Nori, "Landau–Zener–Stückelberg interferometry," Phys. Rep. **492**, 1–30 (2010).

[34] Tatsuhiko N. Ikeda, Satoshi Tanaka, and Yosuke Kayanuma, "Floquet-Landau-Zener interferometry: Usefulness of the Floquet theory in pulse-laser-driven systems," Phys. Rev. Res. **4**, 033075 (2022).

[35] B Kramer and A MacKinnon, "Localization: theory and experiment," Rep. Prog. Phys. **56**, 1469 (1993).

[36] G.M. Zaslavsky, *Hamiltonian Chaos and Fractional Dynamics* (OUP Oxford, 2005).

[37] Sandro Wimberger, *Nonlinear dynamics and quantum chaos: An introduction* (Springer, Berlin, 2014) p. 206.

[38] N B Delone, B P Kraĭnov, and D L Shepelyanskiĭ, "Highly-excited atoms in the electromagnetic field," Sov. phys., Usp. **26**, 551 (1983).

[39] G Casati, "Relevance of classical chaos in quantum mechanics: The hydrogen atom in a monochromatic field," Phys. Rep. **154**, 77–123 (1987).

[40] Kwanghsi Wang and Shih-I Chu, "Dynamics of multiphoton excitation and quantum diffusion in Rydberg atoms," Phys. Rev. A **39**, 1800–1808 (1989).

[41] Albert Messiah, *Quantum mechanics* (Dover Publications, Inc., Garden City, New York, 2020).

[42] P. Kurilovich, T. Connolly, C. Boettcher, S. Diamond, H. Nho, A. Ding, D. Weiss, V. Kurilovich, V. Fatemi, L. Glazman, and M. Devoret, In preparation.

[43] Vladimir E. Manucharyan, Jens Koch, Leonid I. Glazman, and Michel H. Devoret, "Fluxonium: Single Cooper-pair circuit free of charge offsets," Science **326**, 113–116 (2009).

[44] Eric Hyyppä, Suman Kundu, Chun Fai Chan, András Gunyhó, Juho Hotari, David Janzso, Kristinn Juliusson, Olavi Kiuru, Janne Kotilahti, Alessandro Landra, *et al.*, "Unimon qubit," Nat. Commun. **13**, 6895 (2022).

[45] Nicolas Didier, Jérôme Bourassa, and Alexandre Blais, "Fast quantum nondemolition readout by parametric modulation of longitudinal qubit-oscillator interaction," Phys. Rev. Lett. **115**, 203601 (2015).

[46] Alex Chapple, Alexander McDonald, Manuel Muños-Arias, Christian de Correc, Michelle Lachapelle, and Alexandre Blais, In preparation.

[47] S. A. Caldwell, N. Didier, C. A. Ryan, E. A. Sete, A. Hudson, P. Karalekas, R. Manenti, M. P. da Silva, R. Sinclair, E. Acala, N. Alidoust, J. Angeles, A. Bestwick, M. Block, B. Bloom, A. Bradley, C. Bui, L. Capelluto, R. Chilcott, J. Cordova, G. Crossman, M. Curtis, S. Deshpande, T. El Bouayadi, D. Girshovich, S. Hong, K. Kuang, M. Lenihan, T. Manning, A. Marchenkov, J. Marshall, R. Maydra, Y. Mohan, W. O'Brien, C. Osborn, J. Otterbach, A. Papageorge, J.-P. Paquette, M. Pelstring, A. Polloreno, G. Prawiroatmodjo, V. Rawat, M. Reagor, R. Renzas, N. Rubin, D. Russell, M. Rust, D. Scarabelli, M. Scheer, M. Selvanayagam, R. Smith, A. Staley, M. Suska, N. Tezak, D. C. Thompson, T.-W. To, M. Vahidpour, N. Vodrahalli, T. Whyland, K. Yadav, W. Zeng, and C. Rigetti, "Parametrically activated entangling gates using transmon qubits," Phys. Rev. Appl. **10**, 034050 (2018).

[48] A O Niskanen, K Harrabi, F Yoshihara, Y Nakamura, S Lloyd, and J S Tsai, "Quantum coherent tunable coupling of superconducting qubits," Science **316**, 723–726 (2007).

[49] Shruti Puri, Samuel Boutin, and Alexandre Blais, "Engineering the quantum states of light in a Kerr-nonlinear resonator by two-photon driving," npj Quantum Inf. **3**, 18 (2017).

[50] Nicholas E Frattini, Rodrigo G Cortiñas, Jayameenakshi Venkatraman, Xu Xiao, Qile Su, Chan U Lei, Benjamin J Chapman, Vidul R Joshi, S M Girvin, Robert J Schoelkopf, Shruti Puri, and Michel H Devoret, "The squeezed kerr oscillator: spectral kissing and phase-flip robustness," (2022), arXiv:2209.03934 [quant-ph].

[51] Jorge Chávez-Carlos, Rodrigo G Cortiñas, Miguel A Prado Reynoso, Ignacio García-Mata, Victor S Batista, Francisco Pérez-Bernal, Diego A Wisniacki, and Lea F Santos, "Driving superconducting qubits into chaos," (2023), arXiv:2310.17698 [quant-ph].

[52] Benjamin D'Anjou and Guido Burkard, "Optimal dispersive readout of a spin qubit with a microwave resonator," Phys. Rev. B **100**, 245427 (2019).

[53] J. R. Schrieffer and P. A. Wolff, "Relation between the anderson and kondo hamiltonians," Phys. Rev. **149**, 491–492 (1966).

[54] Jon H. Shirley, "Solution of the Schrödinger equation with a Hamiltonian periodic in time," Phys. Rev. **138**,

B979–B987 (1965).